Cluster-State Creation in Liquid-State NMR

by

Jennifer T. Choy

Submitted to the Department of Nuclear Science and Engineering
in partial fulfillment of the requirements for the degree of

Bachelor of Science in Nuclear Science and Engineering

at the

MASSACHUSETTS INSTITUTE OF TECHNOLOGY

June 2007

© Massachusetts Institute of Technology 2007. All rights reserved.

Author ....
Department of Nuclear Science and Engineering
May 18, 2007

Certified by ....
David G. Cory
Professor of Nuclear Science and Engineering
Thesis Supervisor

Accepted by ....
David G. Cory
Chairman, Department Committee on Undergraduate Students

MASSACHUSETTS INSTITUTE OF TECHNOLOGY
OCT 1 2 2007
LIBRARIES

ARCHIVES

Cluster-State Creation in Liquid-State NMR

by

Jennifer T. Choy

Submitted to the Department of Nuclear Science and Engineering
on May 18, 2007, in partial fulfillment of the
requirements for the degree of
Bachelor of Science in Nuclear Science and Engineering

Abstract

The subject of this thesis is devoted to a class of multiparticle entangled states known as the cluster-states. In particular, we focused on a system of four spins and studied the entanglement properties of a four-qubit cluster-state, using a set of entanglement measures for quantifying multipartite entanglement. We then experimentally prepared the linear cluster-state in a liquid NMR sample of crotonic acid, by applying a set of pulses generated by the Gradient Ascent Pulse Engineering (GRAPE) algorithm on a temporally averaged pseudo-pure state of four carbon spins. While our spectral results were consistent with the creation of a linear cluster-state, the reconstruction of the experimental density matrix via a full state tomography of the system revealed additional challenges in the detection of certain desired spin terms. These problems must be overcome before the system could be studied quantitatively.

Thesis Supervisor: David G. Cory
Title: Professor of Nuclear Science and Engineering

Acknowledgments

I would like to first thank Prof. David Cory for all the research opportunities and guidance he has given me over the last four years. I am especially grateful to him for the tremendous and positive impact he has made on my academic career, by introducing me to the field of quantum computing. Despite encountering difficulties in either specific subject materials or general research and academic directions, he has always been extremely supportive, encouraging and infinitely patient.

I would like to thank Troy Borneman for providing the pseudo-pure state preparation sequences and pulses, teaching me the technical aspects of the experiment, and his deep involvement with the project even during the busiest of times. Also a big "thank you" to members of the Cory group, for helpful discussions, support, and always keeping a fun and congenial spirit around the lab.

It's been a blessing to be able to work and become friends with my fellow classmates in Nuclear Science and Engineering and I thank them for their friendship and encouragements.

Finally, I would like to thank my family whose love and presence continue to fuel and inspire me in everything I do.

Contents

1 Introduction **13**

1.1 Entangled states and the measurement-based model of quantum computation 13

1.2 NMR as a quantum information processor 15

1.3 Thesis objective 15

2 Cluster-State Description and Preparation **17**

3 Entanglement Properties of the Four-Qubit Cluster-State **21**

3.1 Bipartite Entanglement 21

3.2 Tripartite entanglement 24

3.3 Four-particle entanglement 25

3.3.1 n-tangle 26

3.3.2 Schmidt decomposition 26

3.3.3 Four-particle entanglement under loss of one qubit 26

3.3.4 Four-particle entanglement under loss of two qubits 27

3.4 Interpretations 29

4 Experimental Cluster-State Preparation and Detection in NMR **33**

4.1 Creation of pseudo-pure state 34

4.2 Pulse sequence 38

4.3 Linear cluster state preparation and results 39

5 Discussion **49**

A Pseudo-Pure State Preparation via Temporal Averaging 51

B GRAPE Algorithm for Pulse Making 55

List of Figures

2-1 Cluster-states or graph-states can be mapped onto a d-dimensional graph where qubits are represented by lattice sites (circled) and the lines that connect neighboring vertices a, a' indicate that H_{int} has been applied to those qubits. 18

2-2 Four-qubit cluster-states. 19

2-3 Quantum circuit for the construction of the box cluster shown in Figure 2-2. Each horizontal wire represents the time-dependent operations on a qubit, with the initial states indicated on the left. H represents the single-qubit Hadamard operation. For two-qubit control operations, the control qubit is indicated by the dot and the operation is shown on the quantum wire for the target qubit. ϕ represents a controlled-PHASE gate. If the last controlled-PHASE operation between qubits 1 and 4 is left out, then the resulting state is the linear cluster. 19

3-1 Quantum network for the creation of an entangled state using two qubits. 22

4-1 Structure of a crotonic acid molecule. The four Carbon-13 nuclei (C_1, C_2, C_3, C_4) comprise our four-qubit system. H denotes proton. 33

4-2 Comparison between the spectrum obtained by applying the Hadamard gate with that obtained with a collective $\frac{\pi}{2}$ pulse around y on all spins. In both cases, the final state is $I_x^1 + I_x^2 + I_x^3 + I_x^4$, which would result in all spins pointing up. 41

4-3 These two spectra compare the action of the $C_1 - PHASE_2$ gate on the equilibrium state and the state $I^1_z + I^2_z$. The C-PHASE gate should have no effect on ρ_{eq} and transform the I_x state into $I^1_z I^2_x + I^1_x I^2_z$. The resulting spectrum for the latter therefore contains two antiphase peaks on spins 1 and 2. 42

4-4 These two spectra compare the action of the $C_2 - PHASE_3$ gate on the equilibrium state and the state $I^2_z + I^3_z$. $(C_2 - PHASE_3)\rho_{eq} = \rho_{eq}$ and $(C_2 - PHASE_3)I^2_z + I^3_z = I^2_z I^3_x + I^2_x I^3_z$. 42

4-5 These two spectra compare the action of the $C_3 - PHASE_4$ gate on the equilibrium state and the state $I^3_z + I^4_z$. 43

4-6 These two spectra compare the action of the $C_4 - PHASE_1$ gate on the equilibrium state and the state $I^1_z + I^4_z$. 43

4-7 (a)-(b) show the experimental and simulated spectra of the carbon system after the linear cluster preparation has been applied to thermal equilibrium; (c)-(d) show the spectra after the linear cluster preparation was applied to the pseudo-pure state term corresponding to $I^1_z I^2_z$, after a $\frac{\pi}{2}$ pulse along x on the first carbon. (e)-(f) show the spectra of the $I^3_z I^4_z$ terms after the linear cluster preparation sequence and a $\frac{\pi}{2}$ pulse along x on the fourth carbon. In the next couple of figures, we provide a spin-by-spin comparison of each of the spectra with simulated results and provide the product operator expression for the states. . . 44

4-8 Spin-by-spin comparison of the experimental detection of the state $I^1_x I^2_z + I^3_z I^4_x + I^1_z I^2_x I^3_z + I^2_z I^3_x I^4_z$ with simulations. This state results from applying the linear cluster preparation to thermal equilibrium. . 45

4-9 Spin-by-spin comparison with simulations of the experimental measurement of the state $I^1_z I^2_x I^3_z + I^2_z I^3_x I^4_z + I^3_z I^4_x + I^1_y I^2_y I^3_z$, with a $\frac{\pi}{2})^1_x$ readout. The final state is $-I^1_y I^2_x I^3_z + I^2_z I^3_x I^4_z + I^3_z I^4_x + I^1_z I^2_y I^3_z$. 46

4-10 Spin-by-spin comparison with simulations of the experimental measurement of the state $I^1_x I^2_z + I^1_z I^2_x I^3_z + I^2_z I^3_x I^4_z + I^2_z I^3_y I^4_y$, with a $\frac{\pi}{2})^4_x$ readout. The final state is $I^1_x I^2_z + I^1_z I^2_x I^3_z - I^2_z I^3_x I^4_y + I^2_z I^3_y I^4_z$. 47

List of Tables

3.1 Global entanglement properties of four-particle entangled states $|\psi\rangle_{box}$, $|\psi\rangle_{linear}$, $|W\rangle$, and $|GHZ\rangle$. This table shows the values of $Q = 2 - \frac{2}{n}\sum_i \mathrm{Tr}\{\rho_i^2\}$, which examines the mixedness of the system under one particle loss, and the Schmidt numbers of various subsystems, which refers to the number of terms in the Schmidt decomposition. 29

3.2 Local (pairwise) entanglement properties of four-particle entangled states $|\psi\rangle_{box}$, $|\psi\rangle_{linear}$, $|W\rangle$, and $|GHZ\rangle$. This table shows the values of the n-tangle (τ_4), the mixed state three-tangles for the four possible three-qubit subsystems (τ_{ABC}, τ_{BCD}, τ_{ACD}, τ_{ABD}), and concurrences C_{AB}, C_{AC}, and C_{AD}. 29

4.1 Table of coefficients for each term in the temporally-averaged pseudo pure state, according to simulation results. The desired terms are in bold print and the numbers in the first column denote the experiment number as shown in Appendix A. 35

4.2 Table of experimental coefficients for each term in the temporally-averaged pseudo pure state. The numbers in the top row correspond to the sequence number of state preparation listed in Appendix A. The coefficients are normalized such that the term with the largest contribution to each state has its coefficient set to one. 37

4.3 Input pseudo pure state terms and the corresponding output states after linear cluster-state preparation. The desired terms are displayed in bold print. 40

B.1 Control parameters input into the GRAPE algorithm. 56

Chapter 1

Introduction

1.1 Entangled states and the measurement-based model of quantum computation

Quantum computation relies on the superposition principle to store and manipulate information with greater efficiency than that achieved by a classical computer. The computational basis in quantum information is known as a qubit, which is analogous to the unit of binary memory in classical computation. Qubits can be physically represented by two-level quantum systems and are expressed in the orthogonal quantum states $|0\rangle$ and $|1\rangle$. It is the superposition of these computational bases that gives a quantum computer an enhanced capability over its classical counterpart, since parallel operations can be performed on all combinations of quantum states at once.

The implementation of quantum computation (QC) involves applying quantum gates and measurements to a set of prepared qubits [1]. A quantum gate is typically a unitary operation that coherently manipulates the superpositions of quantum states. It has been shown that there is a universal set of quantum gates upon which any arbitrary unitary gates can be constructed. This set includes all single-qubit operations and one conditional two-qubit gate, such as the controlled-NOT [2]. For most computations, the outcome needs to be a classical string and so the quantum algorithm ends in a final projective measurement that destroys all quantum superpositions.

There have been experimental demonstrations of the basic principles of quantum computation using various physical implementations, including: ion traps, optical cavities, and nuclear magnetic resonance (NMR). However, the scalability of these models to a system that can match the computational power of current classical computers is hampered by the difficulty of maintaining quantum coherence in the system over the duration of computation. Furthermore, while there exists a universal set of gates, the construction of n-qubit unitary operations requires a number of gates that scales exponentially with the size of the system [3].

To overcome these challenges while building a sizable quantum computer, significant theoretical advances have been made in recent years including error correction [4, 5, 6, 7] and teleportation [8]. Most of these techniques rely upon the concept of entangling measurements, in which the act of measurement on an entangled state transfers quantum information from one place to another, rather than destroying it entirely [9]. Entangled states are therefore valuable resources for QC, especially since they are ubiquitous in large quantum systems.

One specific class of entangled states, the cluster-state or graph state, is generated by Ising-type interactions between neighboring qubits [10, 11]. These states are found naturally in large Hilbert spaces, but can be created in smaller systems by controlling the interactions between selected qubits, using the standard QC methods of applying unitary gates. Cluster-states are ideal systems for implementing quantum teleportation and error correction techniques since they have been shown to be more resilient to disturbances by local operations than other maximally entangled states and have the capacity to teleport multi-qubit entangled states [12, 13].

The entanglement properties of a cluster-state has inspired a new scheme of QC [14], in which information processing proceeds via a series of one-qubit measurements on the cluster-state, followed by conditional gates that are already built into the entangled substrate. Since computation is executed by a set of measurements, this model is known as measurement-based or one-way QC. The special feature of this scheme is that unlike the more conventional models of a quantum computer, such as the quantum network model [15, 16], information is not encoded in the physical qubits, but in the entanglement between the qubits. It has also been shown that for many algorithms, the number of computational steps scales more favorably with the system size than the network model [11].

1.2 NMR as a quantum information processor

In a NMR quantum information processor, qubits are represented by the nuclear spins contained within an ensemble of molecules. NMR is an effective testbed for demonstrating and developing new techniques for QC, due to its long decoherence time (on the order of seconds) relative to the timescales over which unitary evolutions occur. This suggests that that quantum information can be preserved over the course of computation. The application of radiofrequency (RF) pulses in NMR also provides a robust method for coherently controlling the interactions between specific spins in the system, thereby allowing the precise implementation of unitary gates [17].

The realization of a quantum information processor in a NMR system was a challenge at first because spins are in a mixed state at room temperature, whereas QC requires that its system be in a pure state. Proposals for performing QC in such an ensemble system were first given by Cory, Fahmy, and Havel [18] and Gershenfeld and Chuang [19]. The method outlined in [18] involves the creation of pseudo-pure states, which are mixed states that transform similarly to pure spin states.

The highly mixed nature of the spin states renders the extraction of pseudo-pure states for more than ten qubits impractical [18, 20]. However, in the nascent stage of experimentally realizing QC, NMR remains a potent technology for developing methods of control and demonstrating the implementation of standard quantum algorithms.

1.3 Thesis objective

The objective of this thesis is to create a four-qubit cluster-state via liquid-state NMR and to use this state to demonstrate one-way quantum computation in an ensemble system. The creation and detection of the cluster-state can provide interesting insights about the nature of multipartite entanglement, as well as offer an alternative means of performing quantum algorithms in NMR that is perhaps more robust against decoherence and other local effects within the sample.

Chapter 2

Cluster-State Description and Preparation

Entanglement is a special feature of quantum mechanics. It describes a phenomenon by which the quantum states of spatially separated objects become correlated to one another in a way that violates classical expectations. Since it is impossible to define a separate state for each object, measurement of the physical observables in the system would yield correlated results. For this reason, entanglement is a valuable and powerful resource for computation, enabling the transmission of data between qubits (teleportation) and the transfer of error information from a data qubit onto an observable subspace (error detection and correction).

While two-particle (bipartite) entangled states are fairly well-understood and can be easily related to the entanglement contained in a Bell-state [21], there exist inequivalent classes of entangled states for multi-particle systems with three or more parties. For instance, tripartite entanglement falls under either the Werner (W) or the Greenberger-Horne-Zeilinger (GHZ) class [22]. In a four-particle system, new classes of entangled states emerge which contain properties that differ from those of the W and GHZ states. One example is the n-qubit cluster-state which was first introduced by Briegel and Raussendorf [10].

Cluster-states may be generated in arrays of qubits that interact via Ising-type interactions, under the interaction Hamiltonian [10]

$$H_{int} = \hbar g(t) \sum_{a,a'} f(a-a') \frac{1+\sigma_z^{(a)}}{2} \frac{1-\sigma_z^{(a')}}{2}, \tag{2.1}$$

where a and a' represent the lattice sites of the qubits, gf is the coupling strength, and σ_z is the pauli matrix. Cluster-states are part of a larger family of states known as graph states, which are states that can be mapped onto a d-dimensional graph formed by adjoining vertices in which each vertex corresponds to a qubit and connecting graph vertices infer entangled qubits (see Figure 2-1).

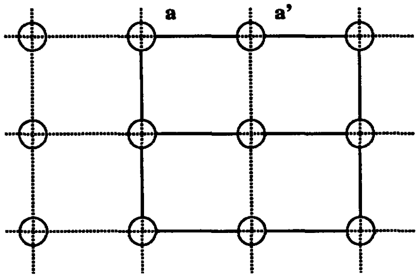

Figure 2-1: Cluster-states or graph-states can be mapped onto a d-dimensional graph where qubits are represented by lattice sites (circled) and the lines that connect neighboring vertices a, a' indicate that H_{int} has been applied to those qubits.

The cluster-states originally conceived by Briegel and Raussendorf and implemented in one-way QC refer to a square lattice array of entangled qubits. With the incorporation of graph states of various geometries in one-way QC schemes, the term "cluster-states" is no longer confined to graph states with a square geometry. To avoid confusion, I will use the term "cluster-state" to describe graph states that are used in one-way computation models.

For a linear array of n entangled qubits, we can simplify the interaction Hamiltonian to

$$H_{int}^{linear} = \hbar g(t) \sum_{a=1}^{n-1} \frac{1+\sigma_z^{(a)}}{2} \frac{1-\sigma_z^{(a+1)}}{2}, \tag{2.2}$$

where we set $\int g(t)\ dt = \pi$, since this condition yields a maximally entangled state (we will define this in a later chapter) [10]. Under this case, the action of H_{int} is equivalent to a controlled-PHASE gate between each pair of qubits a and $a+1$, with the corresponding operator $|0\rangle_a\, {}^a\langle 0| \otimes I^{(a+1)} + |1\rangle_a\, {}^a\langle 1| \otimes \sigma_z^{(a+1)}$. The resulting "graph" corresponding to the mapping of the state onto a geometric plane will have a linear structure.

For a system consisting of four qubits, the cluster-state can have a linear or box configuration, as shown in Figure 2-2. The corresponding circuit for generating such states are shown below in Figure 2-3.

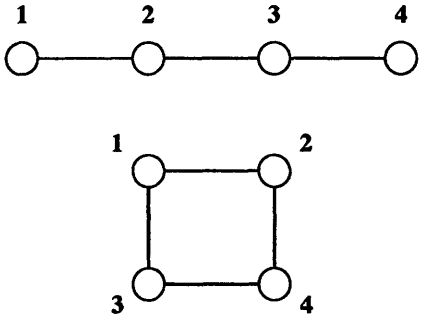

Figure 2-2: Four-qubit cluster-states.

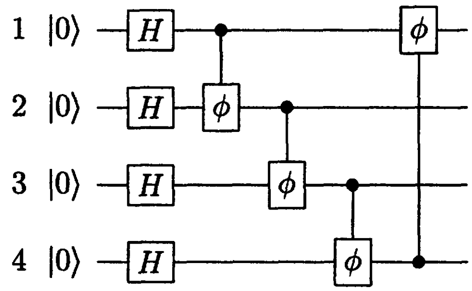

Figure 2-3: Quantum circuit for the construction of the box cluster shown in Figure 2-2. Each horizontal wire represents the time-dependent operations on a qubit, with the initial states indicated on the left. H represents the single-qubit Hadamard operation. For two-qubit control operations, the control qubit is indicated by the dot and the operation is shown on the quantum wire for the target qubit. ϕ represents a controlled-PHASE gate. If the last controlled-PHASE operation between qubits 1 and 4 is left out, then the resulting state is the linear cluster.

As demonstrated in the quantum circuit, the initial state of the system is $|\psi\rangle_{initial} = |0000\rangle$. A Hadamard operation performed on each of the four qubits transforms $|0000\rangle$ into $|++++\rangle$, where $|\pm\rangle = \frac{1}{\sqrt{2}}(|0\rangle \pm |1\rangle)$. This is followed by the application of controlled-PHASE gates, which are two-qubit operations that rotates the target qubit along the $\hat{z}$-axis by π, conditional on the control qubit being in the $|1\rangle$ state. The final state becomes

$$|\psi\rangle_{box} = \frac{1}{2}(|0+0+\rangle + |1-0-\rangle + |0-1-\rangle + |1+1+\rangle) \tag{2.3}$$

for the box geometry. If we leave out the C-PHASE operation between qubits 1 and 4, we obtain the linear cluster which has the form

$$|\psi\rangle_{linear} = \frac{1}{2}(|0+0+\rangle + |1+1-\rangle + |1-0+\rangle + |0-1-\rangle). \tag{2.4}$$

The entanglement property of the linear cluster-state allows us to replace the last C-PHASE gate with the following operation

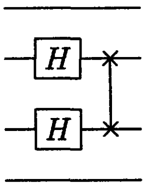

where x-x represents the swap gate. A box cluster-state can therefore be prepared from a linear cluster-state by application of the Hadamard gate on qubits 2 and 3, followed by a swap operation between the two qubits.

Chapter 3

Entanglement Properties of the Four-Qubit Cluster-State

I will now discuss the different entanglement measures that will be used to quantify the degree of entanglement in the four-qubit cluster-state.

3.1 Bipartite Entanglement

An important concept in the classification of entangled states is that entangled states are considered equivalent if they are relatable through local transformations; that is, entanglement properties are invariant under local unitary operations. For bipartite entanglement there exists one class of maximally entangled pure states, which are known as the Bell-states:

$$|\Phi^{\pm}\rangle = \frac{|00\rangle \pm |11\rangle}{\sqrt{2}} \tag{3.1}$$

$$|\Psi^{\pm}\rangle = \frac{|01\rangle \pm |10\rangle}{\sqrt{2}}, \tag{3.2}$$

where we can take $|0\rangle$ and $|1\rangle$ to represent the up and down spin states along $\hat{z}$.

Many methods have been proposed to quantify bipartite entanglement, but scaling these measures to accommodate multipartite entanglement with a larger number of parties is a formidable task due to the complexicity of multipartite entanglement.

Here we use a measure for global entanglement, Q, to study the entanglement structure of the cluster-state under the loss of one qubit, and the methods of mixed three-tangle and concurrence to quantify the remaining tripartite and bipartite entanglement in the system. Two-qubit entanglement will now be explored in greater depth through an example to demonstrate some of these methods.

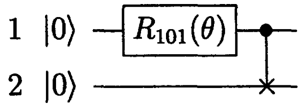

Figure 3-1: Quantum network for the creation of an entangled state using two qubits.

Figure 3-1 shows a set of two operations, with adjustable parameter θ, that can lead to the creation of a two-qubit entangled state. Both qubits 1 and 2 are initially in state $|0\rangle$. The first qubit is subjected to a rotation of θ around the (101) axis for which the corresponding operator is

$$\mathrm{R}_{101}(\theta) = \mathbb{I}\,\cos\frac{\theta}{2} + \frac{i}{\sqrt{2}}(\sigma_1 + \sigma_3)\,\sin\frac{\theta}{2}. \tag{3.3}$$

This rotates the first qubit into some superposition of $|0\rangle$ and $|1\rangle$, depending on the rotation angle θ. The rotation operation is followed by a controlled-NOT gate which flips qubit 2 conditional on qubit 1 being in the $|1\rangle$ state. This results in the state

$$|\psi(\theta)\rangle = (\cos\frac{\theta}{2} + \frac{i}{\sqrt{2}}\sin\frac{\theta}{2})|00\rangle + \frac{i}{\sqrt{2}}\sin\frac{\theta}{2}|11\rangle, \tag{3.4}$$

with corresponding density matrix

$$\begin{aligned}\rho(\theta) =&(\cos^2\frac{\theta}{2} + \frac{1}{2}\sin^2\frac{\theta}{2})|00\rangle\langle 00| + (\frac{i}{\sqrt{2}}\sin\frac{\theta}{2}\cos\frac{\theta}{2} + \frac{1}{2}\sin^2\frac{\theta}{2})|11\rangle\langle 00| \\ &+ (\frac{i}{2\sqrt{2}}\sin\frac{\theta}{2}\cos\frac{\theta}{2} + \frac{1}{2}\sin^2\frac{\theta}{2})|00\rangle\langle 11| + \frac{1}{2}\sin^2\frac{\theta}{2}|11\rangle\langle 11|.\end{aligned} \tag{3.5}$$

It can be shown that $\mathrm{Tr}\{\rho(\theta)^2\} = 1$ and therefore $|\psi(\theta)\rangle$ is a pure state.

To quantify the degree of entanglement contained in the pair of qubits, one can examine the purity of the entangled state under particle loss [23]. In a pure state system, entanglement exists between parts of the system that do not have pure states of their own. For instance, if a state is separable (can be expressed as a single product term) and its separable parts are pure, then it is unentangled.

The partial trace operation is a useful method for examining qubit losses in a system. For a two-qubit state $|\psi\rangle_{\mathrm{AB}}$ with $\rho_{\mathrm{AB}} = |\psi\rangle_{\mathrm{AB}}\ {}_{\mathrm{AB}}\langle\psi|$, the partial trace ρ_{A} is defined by

$$\rho_{\mathrm{A}} = \mathrm{Tr}_{\mathrm{B}}\{\rho_{\mathrm{AB}}\}, \tag{3.6}$$

where Tr_{B} denotes the trace over B. Representing the trace as an inner-product sum, Eqn. (3.6) can be re-written, using the basis $\{|0\rangle_{\mathrm{B}}, |1\rangle_{\mathrm{B}}\}$, as

$$\rho_{\mathrm{A}} = \sum_{i=0}^{1} {}_{\mathrm{B}}\langle i|\rho_{\mathrm{AB}}|i\rangle_{\mathrm{B}}, \tag{3.7}$$

Since the basis set of B is of lower rank than that for the composite system AB, the resulting ρ_A is a reduced density matrix.

Applying Eqn. (3.6) to the pure system in Eqn. (3.5) and tracing over qubit 2, one obtains

$$\rho_{\mathrm{A}}(\theta) = |0\rangle\langle 0|(\cos^2\frac{\theta}{2} + \frac{1}{2}\sin^2\frac{\theta}{2}) + |1\rangle\langle 1|(\frac{1}{2}\sin^2\frac{\theta}{2}). \tag{3.8}$$

It can be shown that $\rho_{\mathrm{A}} = \rho_{\mathrm{B}}$, so the particle over which one traces does not matter. ρ_{A} is a mixed density matrix; the trace of its square yields $\cos^2\frac{\theta}{2} + \frac{1}{4}\sin^2\theta + \frac{1}{2}\sin^4\frac{\theta}{2}$.

We apply the measure for global entanglement $Q = 2 - \frac{2}{\mathrm{n}}\sum_i \mathrm{Tr}\{\rho_i^2\}$ [23, 24], where n denotes the number of qubits in the system and ρ_i represents the partial trace over i, to Eqn. 3.8. Q was introduced as a scalable measure of multiparticle entanglement and has the property of being 0 when the state is a product state and 1 when the state is maximally entangled. When θ is set to $\pi, \frac{3\pi}{2}, \ldots\frac{(2n+1)\pi}{2}$, Q is 1 and the corresponding state in Eqn. 3.4 is that of a Bell-state.

Another measure for bipartite entanglement is the concurrence [25], which is defined as $C = |\langle\phi|\tilde{\phi}\rangle|^2$, where $|\tilde{\phi}\rangle$ denotes the resulting state when the operator $\sigma_y \otimes \sigma_y$ is applied to the complex conjugate of $|\phi\rangle$. For the state $|\psi(\theta)\rangle$, $C = \sqrt{\sin^4\frac{\theta}{2} + \frac{1}{2}\sin^2\theta}$. Like Q, concurrence is also an entanglement monotone that has a maximum value of 1 and is 0 for a factorizable state.

The method for computing C for mixed states is outlined in [26]. It involves first defining the "spin-flipped" matrix as $\tilde{\rho}_{AB} = (\sigma_y \otimes \sigma_y)\rho^*_{AB}(\sigma_y \otimes \sigma_y)$, where * indicates complex conjugation, and then finding the eigenvalues of the product $\rho_{AB}\tilde{\rho}_{AB}$. The concurrence is then given by $C_{AB} = \max\{\lambda_1 - \lambda_2 - \lambda_3 - \lambda_4,\ 0\}$, where the λ's indicate the square roots of the eigenvalues, indexed in descending order.

In general, entanglement monotones conceived for pure states can be extended to mixed states by applying the convex roof formalism [27]. For a mixed state ρ, one can compute the value of an entanglement monotone μ that was originally defined for a pure state $|\psi\rangle$, using

$$\mu_{mixed}(\rho) = \min \sum_i p_i\ \mu(|\psi_i\rangle), \tag{3.9}$$

where $\mu_{mixed}(\rho)$ is the minimum value taken over all possible pure state decompositions $(\sum_i p_i|\psi_i\rangle\langle\psi_i| = \rho)$ of the mixed state system .

3.2 Tripartite entanglement

True tripartite entanglement has two inequivalent classes which are the $|W\rangle$ and the $|GHZ\rangle$ states [22]. These states can be represented by

$$|W\rangle = \frac{1}{\sqrt{3}}(|001\rangle + |010\rangle + |100\rangle) \text{ and} \tag{3.10}$$

$$|GHZ\rangle = \frac{1}{\sqrt{2}}(|000\rangle + |111\rangle). \tag{3.11}$$

The two states are not relatable by local transformations and behave differently under particle losses. While the entanglement in the GHZ state is vulnerable to even the loss of one particle (the state becomes fully mixed and thus completely unentangled when one particle is traced out), the W state retains the maximal amount of entanglement under particle loss, in comparison to other three-qubit entangled states [22].

To quantify tripartite entanglement, the three-tangle (τ_{ABC}) [26] is often used. This measure is based on the method of concurrence for two-particle entanglements and can be computed by considering the entanglement in a system ρ_{ABC} between qubit A and subsystem BC, as well as the shared entanglement between qubits A and B and between A and C. In a pure state system, τ_{ABC} can be calculated from

$$\tau_{ABC} = C^2_{A(BC)} - C^2_{AB} - C^2_{AB}, \tag{3.12}$$

where C^2_{AB} and C^2_{AC} are the concurrences for the reduced density matrices ρ_{AB} and ρ_{AC}. $C^2_{A(BC)}$ considers the entanglement between qubit A and subsystem BC and is equal to 4 detρ_A. The special feature of the three-tangle is that it is at its maximum value of 1 when applied to the $|GHZ\rangle$ state and is 0 for the $|W\rangle$ state [22].

3.3 Four-particle entanglement

There exist nine inequivalent entanglement classes in a four-qubit system [28]. Here we compare the entanglement properties of a cluster-state to those of the other maximally-entangled four-qubit, namely the $|W\rangle$ and $|GHZ\rangle$ states. These states are given by

$$|W\rangle = \frac{1}{2}(|0001\rangle + |0010\rangle + |0100\rangle + |1000\rangle) \tag{3.13}$$

$$|GHZ\rangle = \frac{1}{\sqrt{2}}(|0000\rangle + |1111\rangle). \tag{3.14}$$

In the subsequent sections, we use the method of partial trace to obtain reduced density matrices for the cluster-state system under one or two particle losses. We then apply Q and perform pure state decomposition on the reduced density matrix to quantitatively study the residual entanglement in the system, using the measures of three-tangle (for residual tripartite entanglement) and concurrence (for residual bipartite entanglement). The process of purification is shown rather explicitly due to its relationship to the Schmidt decomposition, which is another useful measure for multipartite entanglement.

3.3.1 n-tangle

The measure of concurrence has been generalized to quantify the entanglement in multiparticle systems with an even number of qubits. This measure is known as the n-tangle [29] and is defined as $\tau_n = |\langle\psi|\tilde{\psi}\rangle|^2$, where $|\tilde{\psi}\rangle = \sigma_y^{\otimes n}|\psi^*\rangle$. When applied to the aforementioned states, $\tau_n = 0$ except for the GHZ state, for which τ_n has a value of 1.

3.3.2 Schmidt decomposition

Any pure state $|\psi\rangle$ of composite system AB can be decomposed into a sum of orthogonal bases for subsystems A and B:

$$|\psi\rangle = \sum_i \lambda_i |i_A\rangle |i_B\rangle, \tag{3.15}$$

where λ_i are called the Schmidt coefficients and have non-negative and real values. The number of terms in the decomposition (known as the Schmidt number) is preserved under local unitary transformations and is thus used as an entanglement monotone. The Schmidt number is 1 for a factorizable state and increases with the amount of entanglement in the system. The Schmidt decomposition is relatable to purification in that purifying a mixed system is equivalent to diagonalizing the mixed density matrix using the Schmidt bases [30].

3.3.3 Four-particle entanglement under loss of one qubit

For the $|\psi\rangle_{box}$ state, four different mixed density matrices (ρ^{box}_{BCD}, ρ^{box}_{ACD}, ρ^{box}_{ABD}, ρ^{box}_{ABC}) result from the loss of one qubit. Each of these matrices is fully mixed ($\mathrm{Tr}\{\rho_{\mathrm{xxx}}^{\mathrm{box}^2}\} = \frac{1}{2}$) and so the measure for global entanglement (Q) for this system is 1. Upon pure state decomposition, the density matrices can be expressed by the sum of two systems, both of which are pure. If either qubit A or qubit C is traced out, each of the terms in the decomposition is formed by a pure state that belongs to the three-qubit GHZ class. For instance, purification of ρ^{box}_{BCD} gives

$$\rho^{box}_{BCD} = \frac{1}{4}[(|+0+\rangle+|-1-\rangle)(\langle+0+|+\langle-1-|)+(|+1+\rangle+|-0-\rangle)(\langle+1+|+\langle-0-|)]. \tag{3.16}$$

In Eqn. 3.16, each pure state is weighed with a coefficient of $\frac{1}{2}$. The state that forms the first subsystem, $|\psi\rangle_a = \frac{1}{\sqrt{2}}(|+0+\rangle + |-1-\rangle)$, is equivalent to the $|GHZ\rangle$ state under the local unitary $H \otimes I \otimes H$, while $|\psi\rangle_b = \frac{1}{\sqrt{2}}(|+1+\rangle + |-0-\rangle)$ can be converted to $|GHZ\rangle$ by the operation $H \otimes \sigma_x \otimes H$. Similar relations can be found for the purification of ρ_{ABD}.

Meanwhile, when qubit B or D is traced out, the resulting system can be purified into two terms each containing a pure state formed by the product between a Bell-state and a single qubit state. For example,

$$\begin{aligned}\rho^{box}_{ACD} &= \frac{1}{4}[(|00+\rangle + |11+\rangle)(\langle 00+| + \langle 11+|) + (|01-\rangle + |10-\rangle)(\langle 01-| + \langle 10-|)] \\ &= \frac{1}{2}(|\Phi^+\rangle\langle\Phi^+| \otimes |+\rangle\langle+| + |\Psi^+\rangle\langle\Psi^+| \otimes |-\rangle\langle-|).\end{aligned} \tag{3.17}$$

The decomposition of the linear cluster with the loss of one qubit is equivalent to that of the box cluster, under the permutations of spins, and yields the same value of 1 for Q.

For the $|GHZ\rangle$ state, tracing out any one qubit gives the reduced density matrix $\rho^{GHZ}_{\mathrm{xxx}} = \frac{1}{2}(|000\rangle\langle000| + |111\rangle\langle111|)$, for which $Q = 1$. The purification of the system yields pure states that are entirely unentangled.

The resulting system from tracing out any one qubit in a four-qubit $|W\rangle$ state can be written as $\rho^{W}_{\mathrm{xxx}} = \frac{1}{4}(3|W\rangle\langle W| + |000\rangle\langle000|)$. For this density matrix, $\mathrm{Tr}\{\rho^{\mathrm{W}\,2}_{\mathrm{xxx}}\} = \frac{5}{8}$ and $Q = \frac{3}{4}$.

3.3.4 Four-particle entanglement under loss of two qubits

Measures that consider the remaining entanglement of the system under the loss of any two spins have three values. For the box cluster state, the reduced matrices

ρ^{box}_{AB}, ρ^{box}_{CD}, ρ^{box}_{AD}, ρ^{box}_{BD} can be written in the form

$$\begin{aligned}\rho^{box}_{AB} &= \frac{1}{4}(|0+\rangle\langle 0+| + |1+\rangle\langle 1+| + |0-\rangle\langle 0-| + |0-\rangle\langle 0-|) \\ &= \frac{1}{4}[(|0\rangle\langle 0| + |1\rangle\langle 1|) \otimes (|+\rangle\langle +| + |-\rangle\langle -|)] = \frac{1}{4}\mathbb{I}.\end{aligned} \tag{3.18}$$

On the other hand, ρ^{linear}_{AC} and ρ^{linear}_{BD} can be purified into

$$\rho^{box}_{AC} = \frac{1}{2}(|\Phi^+\rangle\langle\Phi^+| + |\Psi^+\rangle\langle\Psi^+|). \tag{3.19}$$

Applying the method of concurrence to these reduced systems gives a value of 0 for all decompositions.

In the linear cluster, pure state decomposition of the reduced two-qubit system ρ^{linear}_{AB} results in

$$\rho^{linear}_{AB} = \frac{1}{4}[(|0+\rangle + |1-\rangle)(\langle 0+| + \langle 1-|) + |0-\rangle\langle 0-| + |1+\rangle\langle 1+|]. \tag{3.20}$$

Applying the operation $I \otimes H$ on ρ^{linear}_{AB} gives the expression $\tilde{\rho}^{linear}_{AB} = \frac{1}{4}(2\;|\Phi^+\rangle\langle\Phi^+| + |01\rangle\langle 01| + |10\rangle\langle 10|)$. Similar decompositions can be performed on the other two-qubit mixed subsystems. The two-qubit systems have concurrences of 0.

Meanwhile, The mixed subsystem remaining in the $|W\rangle$ state after the disposal of any two qubits can be decomposed into

$$\rho^{W}_{xx} = \frac{1}{2}(|\Phi^+\rangle\langle\Phi^+| + |00\rangle\langle 00|), \tag{3.21}$$

for which $C = 1$. For the $|GHZ\rangle$ state, the remaining system can be represented by

$$\rho^{GHZ}_{xx} = \frac{1}{2}(|00\rangle\langle 00| + |11\rangle\langle 11|), \tag{3.22}$$

where $C = 0$.

Tables 3.1 and 3.2 summarize the entanglement measures used in this chapter and provide their values for each of the four-qubit entangled states we studied.

Table 3.1: Global entanglement properties of four-particle entangled states $|\psi\rangle_{box}$, $|\psi\rangle_{linear}$, $|W\rangle$, and $|GHZ\rangle$. This table shows the values of $Q = 2 - \frac{2}{n}\sum_{i} \mathrm{Tr}\{\rho_i^2\}$, which examines the mixedness of the system under one particle loss, and the Schmidt numbers of various subsystems, which refers to the number of terms in the Schmidt decomposition.

	Q	Schmidt Number			
State		$\rho_{A(BCD)}$	$\rho_{(AB)(CD)}$	$\rho_{(AC)(BD)}$	$\rho_{(AD)(BC)}$
$\|\psi\rangle_{box}$	1	2	4	2	4
$\|\psi\rangle_{linear}$	1	2	3	3	3
$\|W\rangle$	$\frac{3}{4}$	2	2	2	2
$\|GHZ\rangle$	1	2	2	2	2

Table 3.2: Local (pairwise) entanglement properties of four-particle entangled states $|\psi\rangle_{box}$, $|\psi\rangle_{linear}$, $|W\rangle$, and $|GHZ\rangle$. This table shows the values of the n-tangle (τ_4), the mixed state three-tangles for the four possible three-qubit subsystems (τ_{ABC}, τ_{BCD}, τ_{ACD}, τ_{ABD}), and concurrences C_{AB}, C_{AC}, and C_{AD}.

State	τ_4	τ_{ABC}	τ_{BCD}	τ_{ACD}	τ_{ABD}	C_{AB}	C_{AC}	C_{AD}
$\|\psi\rangle_{box}$	0	0	1	0	1	0	0	0
$\|\psi\rangle_{linear}$	0	0	1	1	0	0	0	0
$\|W\rangle$	0	0	0	0	0	$\frac{1}{2}$	$\frac{1}{2}$	$\frac{1}{2}$
$\|GHZ\rangle$	1	0	0	0	0	0	0	0

3.4 Interpretations

Entanglement measures tell us to what degree a system is entangled, which is directly related to the usefulness of the system in quantum computation. The entanglement contained in multipartite states (pure or mixed) beyond two qubits becomes increasingly difficult to characterize and often one needs to perform more than one measure to distinguish among several inequivalent classes. There are many possibilities in identifying a suitable set of entanglement measures for a given system. The Schmidt measure is an entanglement monotone that is computed from the $\log_2$ of the Schmidt number. It was used in [31] to examine four-qubit entangled states, including the cluster-state, $|W\rangle$, and $|GHZ\rangle$. The results obtained in that study are consistent with those shown in Table 3.1.

In this chapter, a nine-parameter approach was used to characterize the entanglement in a four-qubit cluster state. While the Schmidt measure compares the separability of a state under different partitions, the method used here makes the distinction between high-order entanglement, which can be seen as the global entanglement shared among all parties in the system, and the pairwise, or residual, entanglement of the system under qubit losses.

Q is an effective way of discerning global entanglement because it measures the degree of "mixedness" in the remaining system under the disposal of any one of the four qubits. Out of the four states we studied, only the $|W\rangle$ exhibits partial global entanglement, all the other states have a maximal Q value of 1.

The results of the four-qubit n-tangle is similar to those found in the three-tangle case, τ_4 is 1 for a $|GHZ\rangle$ state and vanishes for the $|W\rangle$ state. The cluster-state also has a vanishing 4-tangle.

The residual entanglement of the system under particle loss is studied using the mixed three-tangle method and the two-particle concurrence. They both measure the robustness of a state against the loss of a qubit. For the $|GHZ\rangle$ state, even though the system has maximal four-partite entanglement, tracing out one qubit completely destroys all the residual entanglement in the system (as τ_{ABC} and C vanish for the remaining mixed systems). The $|W\rangle$ also has values of 0 for its mixed three-tangle, but it contains partial bipartite entanglement ($C = \frac{1}{2}$).

For the box and linear cluster states, true tripartite entanglement remains in some cases. This follows from the purification result. The mixed system from tracing out qubit A or C can be decomposed into two pure state systems that are locally equivalent to a $|GHZ\rangle$ state, for which $\tau_{ABC} = 1$. If one defines the average three-tangle as $\tau_3^{avg} = \frac{1}{4}(\tau_{ABC} + \tau_{ABD} + \tau_{ACD} + \tau_{BCD})$, its value is $\frac{1}{2}$ for both cluster-states and 0 for the $|GHZ\rangle$ and $|W\rangle$ states. However, the cluster-states lose all bipartite entanglement upon the disposal of two qubits, as the concurrence vanishes for all decompositions.

We therefore find that a combination of nine entanglement measures is sufficient to distinguish the cluster-state from the $|W\rangle$ and $|GHZ\rangle$ states. By studying the higher-order (global) and residual entanglement in the systems, one can see that the cluster-state exhibits properties belonging to both the W and GHZ class. However, unlike both the $|W\rangle$ and the $|GHZ\rangle$ states, it retains some true tripartite entanglement under one qubit loss.

Chapter 4

Experimental Cluster-State Preparation and Detection in NMR

The set of operations for the creation of the cluster-state was implemented in liquid-state NMR and applied to a sample of Crotonic acid ($C_4H_6O_2$). The structure of a crotonic acid molecule is shown in Figure 4-1. In the molecule, the internal Hamiltonian for the carbon subsystem (with proton decoupling) can be described by [32]

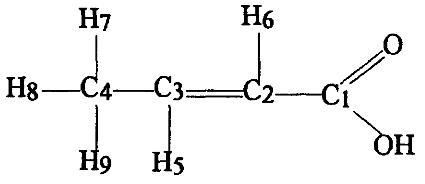

Figure 4-1: Structure of a crotonic acid molecule. The four Carbon-13 nuclei (C_1, C_2, C_3, C_4) comprise our four-qubit system. H denotes proton.

$$H_{int} = \sum_{i=1}^{4} \Omega_i(\vec{r}) I_z^i + 2\pi \sum_{i=1}^{4} \sum_{j=i+1}^{4} J_{ij} \vec{I^i} \cdot \vec{I^j}, \tag{4.1}$$

where $\Omega_i(\vec{r})$ represents the chemical shift of the i-th spin at location $\vec{r}$; J_{ij} is the scalar coupling between spins i and j; and I^i is the angular momentum operator (defined as $\vec{I} = \frac{1}{2}\vec{\sigma}$, where $\vec{\sigma}$ is the pauli matrix vector). The J-coupling constants are: $J_{12} = 75.55\ Hz$, $J_{23} = 69.75\ Hz$, $J_{34} = 41.6\ Hz$, $J_{13} = -1.3\ Hz$, $J_{24} = -1.6\ Hz$, and $J_{14} = 7.1\ Hz$.

All experiments were conducted using a Bruker 400 MHz NMR Spectrometer. We prepared the cluster-state using the four carbon nuclei in the molecule, by applying a series of RF pulses, gradients, and delays. The pulse sequence we used is based on the set of unitary operations illustrated in the quantum circuit in Figure 2-3, in which each input qubit is represented by one of the carbon spins in the liquid NMR system. We implemented the single qubit operations in the circuit by applying RF pulses generated using the GRAPE algorithm [33] to rotate spins. Meanwhile, entangling operations between two qubits were performed also with the application of GRAPE pulses, with pulse times set to match the spin-spin coupling between the carbon nuclei. Non-unitary operations, which are necessary in the creation of the pseudo-pure state, were done with the use of gradients.

4.1 Creation of pseudo-pure state

The realization of a cluster-state in the four carbon system was preceded by the creation of the pseudo pure state from thermal equilibrium ($\rho_{eq} \approx \frac{1}{8}(I_z^1 + I_z^2 + I_z^3 + I_z^4)$, where we have removed the identity $\mathbb{I}$ from the expression). The pseudo pure state has the form

$$\begin{aligned}\rho_{pp} = \frac{1}{16}\mathbb{I}^{\otimes 4} &+ \frac{1}{8}(I_z^1 + I_z^2 + I_z^3 + I_z^4) \\ &+ \frac{1}{4}(I_z^1 I_z^2 + I_z^1 I_z^3 + I_z^1 I_z^4 + I_z^2 I_z^3 + I_z^2 I_z^4 + I_z^3 I_z^4) \\ &+ \frac{1}{2}(I_z^1 I_z^2 I_z^3 + I_z^1 I_z^2 I_z^4 + I_z^1 I_z^3 I_z^4 + I_z^2 I_z^3 I_z^4) \\ &+ I_z^1 I_z^2 I_z^3 I_z^4. \end{aligned} \tag{4.2}$$

With the large number of terms in the density matrix, the observed signals in the readout spectra will be low due to distributed magnetization. For this reason, each term (aside from the identity) was prepared separately and the resulting spectra from each preparation were computationally added to give the full spectra of the pseudo pure system. This method is known as temporal averaging and the pulse sequences used for generating each pseudo-pure state term are given in Appendix A. Table 4.1 shows the relative weighting of each term to construct the full state, based on simulation results.

Table 4.1: Table of coefficients for each term in the temporally-averaged pseudo pure state, according to simulation results. The desired terms are in bold print and the numbers in the first column denote the experiment number as shown in Appendix A.

Sequence number	Pseudo-pure state terms	Coefficient for weighting
1	$-I_z^1$	2.05
2	$-I_z^2$	6.12
3	$-I_z^3$	12.20
4	$-I_z^4$	13.41
5	$I_z^2,\ I_z^3,\ I_z^4,\ \mathbf{I_z^1 I_z^2}$	5.15
6	$-I_z^1,\ I_z^3,\ I_z^4,\ \mathbf{I_z^2 I_z^3}$	3.07
7	$I_z^1,\ I_z^2,\ I_z^3,\ \mathbf{I_z^3 I_z^4}$	2.05
8	$I_z^3,\ I_z^4,\ -I_z^2,\ \mathbf{I_z^1 I_z^3}$	1.05
9	$-I_z^1,\ -I_z^2,\ -I_z^2 I_z^3,\ \mathbf{I_z^2 I_z^4}$	1.07
10	$I_z^4,\ -I_z^1 I_z^2,\ -I_z^3 I_z^4,\ \mathbf{I_z^1 I_z^4}$	1.05
11	$I_z^1,\ I_z^3,\ I_z^4,\ \mathbf{I_z^1 I_z^2 I_z^3}$	2.04
12	$I_z^1,\ I_z^2,\ -I_z^2 I_z^3,\ \mathbf{I_z^2 I_z^3 I_z^4}$	1.05
13	$I_z^1,\ -I_z^1 I_z^2,\ -I_z^1 I_z^2 I_z^3,\ \mathbf{I_z^1 I_z^2 I_z^4}$	1.07
14	$I_z^4,\ -I_z^1 I_z^2,\ I_z^3 I_z^4,\ \mathbf{I_z^1 I_z^3 I_z^4}$	1.05
15	$I_z^1,\ I_z^4,\ -I_z^3 I_z^4,\ \mathbf{I_z^1 I_z^2 I_z^3 I_z^4}$	1.03

Each sequence shown in Appendix A was implemented experimentally using pulses generated by the GRAPE algorithm. A full state tomography, consisting of a set of 18 readout pulses, was then performed on the system. The acquired spectra were recorded and the data was subsequently processed in MATLAB using a tomography code to reconstruct the experimental state density matrix. The product operator decompositions of the density matrix can be found in Table 4.2.

Our experimental data deviates from simulation results in several ways. First, a sign flip was introduced to the coefficient of the target term during the state preparation sequences for $I_z^2 I_z^4$, $I_z^1 I_z^3$, $I_z^1 I_z^2 I_z^4$, and $I_z^1 I_z^2 I_z^3 I_z^4$. This sign flip might be due to a systematic phase error in the sample information used for the GRAPE pulse making process and the simulations. Additionally, the product operator decomposition shows that all three-body terms ($I_z^1 I_z^2 I_z^3$, $I_z^1 I_z^3 I_z^4$, $I_z^1 I_z^2 I_z^4$, $I_z^2 I_z^3 I_z^4$) have either small contributions or are missing in the final state. One possibility is that the curve fitting step during the tomography process cannot resolve the antiphase peaks formed by the weak coupling between non-neighboring spins (for instance, carbons 1 and 3 have a J-coupling of only -1.3 Hz between them). While the missing terms prevent us from being able to compute the weightings for the construction of the full state, we can nonetheless show that our state contains the desired terms by inferring from the spectra under various readout pulses.

Table 4.2: Table of experimental coefficients for each term in the temporally-averaged pseudo pure state. The numbers in the top row correspond to the sequence number of state preparation listed in Appendix A. The coefficients are normalized such that the term with the largest contribution to each state has its coefficient set to one.

Term	1	2	3	4	5	6	7	8	9	10	11	12	13	14	15
I_z^1	-1					-1	1		-1		0.99	0.90	1		1
I_z^2		-1			1		0.99		-0.61			1	-0.65		
I_z^3			-1		0.75	0.95	0.95	1			0.94				
I_z^4				-1	0.81	0.97		0.98		1	1			1	0.88
$I_z^1 I_z^2$					0.79			-0.84		-0.82				-0.82	
$I_z^2 I_z^3$						0.75			-0.68			-0.71			
$I_z^3 I_z^4$							0.80			-0.78				1	-0.79
$I_z^1 I_z^3$								-0.64							
$I_z^2 I_z^4$									-0.67						
$I_z^1 I_z^4$										0.78					
$I_z^1 I_z^2 I_z^3$											0.37		-		
$I_z^2 I_z^3 I_z^4$												-			
$I_z^1 I_z^2 I_z^4$													-0.26		
$I_z^1 I_z^3 I_z^4$														-	
$I_z^1 I_z^2 I_z^3 I_z^4$															-0.72

4.2 Pulse sequence

To implement the sequence for creating a cluster-state, the quantum gates shown in Figure 2-3 were expressed in terms of unitary operations and input into the GRAPE pulse finding code (Appendix B), which searches for the appropriate pulses for carrying out the operations.

The Hadamard transform can be represented by

$$U_H = H \otimes H \otimes H \otimes H, \tag{4.3}$$

in which $H = \frac{1}{\sqrt{2}}(\sigma_x + \sigma_z)$ is the Hadamard operator. In terms of the pauli matrices, the Hadamard transform is

$$U_H = e^{\sum_{i=1}^{4} i\frac{\pi}{2}(\mathbb{I} - \frac{1}{\sqrt{2}}(\sigma_x^i + \sigma_z^i))}. \tag{4.4}$$

This is equivalent to a collective π rotation around the (101) axis on all four spins. The C$_i$-PHASE$_j$ gate, on the other hand, is given by

$$U_\phi(i,j) = E_+^i \otimes \mathbb{I}^j + E_-^i \otimes \sigma_x^j = e^{-i\frac{\pi}{4}\mathbb{I}^{\otimes 4}} e^{i\frac{\pi}{4}\sigma_z^i} e^{i\frac{\pi}{4}\sigma_z^j} e^{-i\frac{\pi}{4}\sigma_z^i\sigma_z^j}, \tag{4.5}$$

where $E_+ = |0\rangle\langle 0|$, $E_- = |1\rangle\langle 1|$, and the kronecker product $\otimes$ between operators applied to different spins is implied in the last expression. Eqn. 4.5 is consistent with the unitary evolution $e^{iH_{int}t}$, where H_{int} is the Ising-type interaction Hamiltonian shown in Eqn. 2.1.

The overall unitary operator for preparing a four-qubit cluster-state from an initial state of $|0000\rangle$ is therefore

$$U_{cluster} = U_\phi(4,1)U_\phi(3,4)U_\phi(2,3)U_\phi(1,2)U_H. \tag{4.6}$$

Meanwhile, the density matrix evolves from an initial density matrix $\rho(0)$ according to

$$\rho(t) = U\rho(0)U^{\dagger}. \tag{4.7}$$

Applying Eqn. 4.6 onto the pseudo-pure state, the density matrix becomes

$$\begin{aligned}\rho_{box} = \frac{1}{16}\mathbb{I}^{\otimes 4} &+ \frac{1}{4}(I_x^1 I_x^3 + I_x^2 I_x^4) + \frac{1}{2}(I_z^1 I_x^2 I_z^3 + I_z^2 I_x^3 I_z^4 + I_x^1 I_z^2 I_z^4 + I_z^1 I_z^3 I_x^4) \\ &+ \frac{1}{2}(-I_y^1 I_x^2 I_y^3 - I_y^2 I_x^3 I_y^4 - I_x^1 I_y^2 I_y^4 - I_y^1 I_y^3 I_x^4) \\ &+ I_z^1 I_z^2 I_y^3 I_y^4 + I_z^2 I_y^2 I_y^3 I_z^4 + I_y^1 I_z^2 I_z^3 I_y^4 + I_y^1 I_y^2 I_z^3 I_z^4 + I_x^1 I_x^2 I_x^3 I_x^4.\end{aligned} \tag{4.8}$$

If the last C-Phase operation between spins 1 and 4 is left out, the resulting density operator corresponds to a linear cluster-state:

$$\begin{aligned}\rho_{linear} = \frac{1}{16}\mathbb{I}^{\otimes 4} &+ \frac{1}{8}(I_x^1 I_z^2 + I_z^3 I_x^4) + \frac{1}{4}(I_z^1 I_x^2 I_z^3 + I_z^2 I_x^3 I_z^4 + I_z^1 I_x^2 I_x^4 + I_y^1 I_y^2 I_z^3) \\ &+ \frac{1}{4}(I_z^2 I_y^3 I_y^4 + I_x^1 I_x^3 I_z^4 + I_y^1 I_y^2 I_x^4 + I_x^1 I_y^3 I_y^4) \\ &+ I_z^1 I_y^2 I_y^3 I_z^4 + I_x^2 I_z^2 I_z^3 I_x^4 - I_z^1 I_y^2 I_x^3 I_y^4 - I_y^1 I_x^2 I_y^3 I_z^4 + I_y^1 I_x^2 I_x^3 I_y^4.\end{aligned} \tag{4.9}$$

The pulse performances of the Hadamard transform and C-Phase gates were first evaluated by observing the resulting spectra for a couple of representative input states. A more quantitative method would be to perform a full state tomography on a number of input states and compare the results with expectations, but this was not done due to time constraints. The representative spectra for the U_H and each of the phase gates are shown in Figures 4-2-4-6.

4.3 Linear cluster state preparation and results

By inspecting the spectra, we found that while the phase gates generally perform the expected actions on their target spins, they also tend to introduce errors into the other carbon spins. These errors appear to be larger for longer pulses ($C_3 - PHASE_4$ and $C_4 - PHASE_1$). We therefore created the linear cluster state, which does not require the $C_4 - PHASE_1$ operation.

The linear cluster state pulse sequence was applied to each term from the pseudo pure state preparation and a full tomography was performed on the resulting states. Table 4.3 shows the simulated input pseudo-pure state terms and the corresponding output states. The problem with the detection of three-body terms encountered in the measurement of the pseudo-pure state again shows up here. Since the entangling operations transform all two-body terms into either three-body or four-body terms, they become difficult to be resolved by tomography and the resulting correlation between the experimental density matrix of each term in Table 4.3 and its theoretical value is poor. However, this is not necessarily an indication that we have failed to create a linear cluster-state. We observed a couple of recorded spectra from tomography and found them to be consistent with simulated spectra (see Figures 4-7-4-8).

Table 4.3: Input pseudo pure state terms and the corresponding output states after linear cluster-state preparation. The desired terms are displayed in bold print.

Input state	Linear cluster-state term
$\rho_{\mathbf{eq}}$	$\mathbf{I_x^1 I_z^2 + I_z^3 I_x^4 + I_z^1 I_x^2 I_z^3 + I_z^2 I_x^3 I_z^4}$
$-I_z^1$	$-I_x^1 I_z^2$
$-I_z^2$	$-I_z^1 I_x^2 I_z^3$
$-I_z^3$	$-I_z^2 I_x^3 I_z^4$
$-I_z^4$	$-I_z^3 I_x^4$
$I_z^2 + I_z^3 + I_z^4 + \mathbf{I_z^1 I_z^2}$	$I_z^1 I_x^2 I_z^3 + I_z^2 I_x^3 I_z^4 + I_z^3 I_x^4 + \mathbf{I_y^1 I_y^2 I_z^3}$
$-I_z^1 + I_z^3 + I_z^4 + \mathbf{I_z^2 I_z^3}$	$-I_x^1 I_z^2 + I_z^2 I_x^3 I_z^4 + I_z^3 I_x^4 + \mathbf{I_z^1 I_y^2 I_y^3 I_z^4}$
$I_z^1 + I_z^2 + I_z^3 + \mathbf{I_z^3 I_z^4}$	$I_x^1 I_z^2 + I_z^1 I_x^2 I_z^3 + I_z^2 I_x^3 I_z^4 + \mathbf{I_z^2 I_y^3 I_y^4}$
$I_z^3 + I_z^4 - I_z^2 + \mathbf{I_z^1 I_z^3}$	$I_z^2 I_x^3 I_z^4 + I_z^3 I_x^4 - I_y^1 I_y^2 I_z^3 + \mathbf{I_x^1 I_x^3 I_z^4}$
$-I_z^1 - I_z^2 - I_z^2 I_z^3 + \mathbf{I_z^2 I_z^4}$	$-I_x^1 I_z^2 - I_z^1 I_x^2 I_z^3 - I_z^1 I_y^2 I_y^3 I_z^4 + \mathbf{I_z^1 I_x^2 I_z^4}$
$I_z^4 - I_z^1 I_z^2 - I_z^3 I_z^4 + \mathbf{I_z^1 I_z^4}$	$I_z^3 I_x^4 - I_y^1 I_y^2 I_z^3 - I_z^3 I_y^3 I_y^4 + \mathbf{I_x^1 I_z^2 I_z^3 I_x^4}$
$I_z^1 + I_z^3 + I_z^4 + \mathbf{I_z^1 I_z^2 I_z^3}$	$I_x^1 I_z^2 + I_z^2 I_x^3 I_z^4 + I_z^3 I_x^4 - \mathbf{I_y^1 I_x^2 I_y^3 I_z^4}$
$I_z^1 + I_z^2 - I_z^2 I_z^3 + \mathbf{I_z^2 I_z^3 I_z^4}$	$I_x^1 I_z^2 + I_z^1 I_x^2 I_z^3 - I_z^1 I_y^2 I_y^3 I_z^4 - \mathbf{I_z^1 I_y^2 I_x^3 I_y^4}$
$I_z^1 - I_z^1 I_z^2 - I_z^1 I_z^2 I_z^3 + \mathbf{I_z^1 I_z^2 I_z^4}$	$I_x^1 I_z^2 - I_y^1 I_y^2 I_z^3 + I_y^1 I_x^2 I_y^3 I_z^4 + \mathbf{I_y^1 I_y^2 I_x^4}$
$I_z^4 - I_z^1 I_z^2 + I_z^3 I_z^4 + \mathbf{I_z^1 I_z^3 I_z^4}$	$I_z^3 I_x^4 - I_y^1 I_y^2 I_z^3 + I_z^2 I_y^3 I_y^4 + \mathbf{I_x^1 I_y^3 I_y^4}$
$I_z^1 + I_z^4 - I_z^3 I_z^4 + \mathbf{I_z^1 I_z^2 I_z^3 I_z^4}$	$I_x^1 I_z^2 + I_z^3 I_x^4 + I_z^2 I_y^3 I_y^4 + \mathbf{I_y^1 I_x^2 I_x^3 I_y^4}$

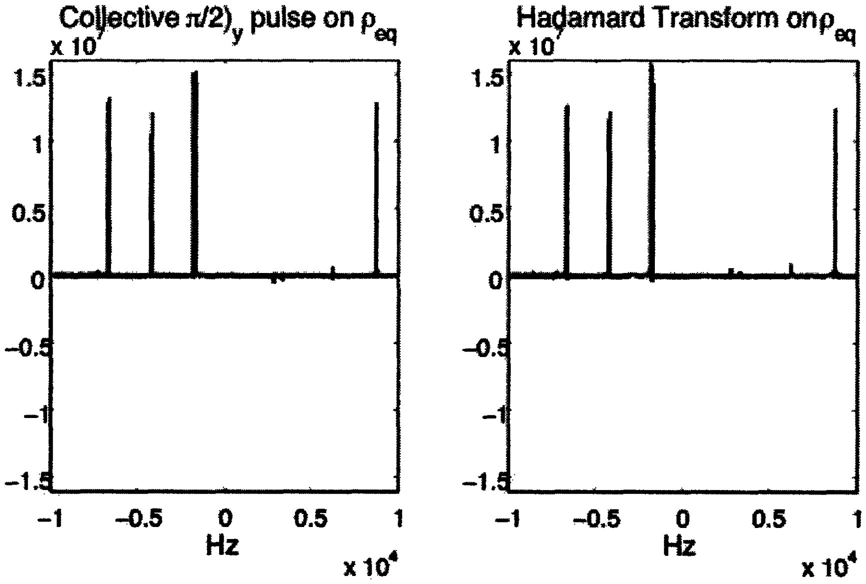

Figure 4-2: Comparison between the spectrum obtained by applying the Hadamard gate with that obtained with a collective $\frac{\pi}{2}$ pulse around y on all spins. In both cases, the final state is $I_x^1 + I_x^2 + I_x^3 + I_x^4$, which would result in all spins pointing up.

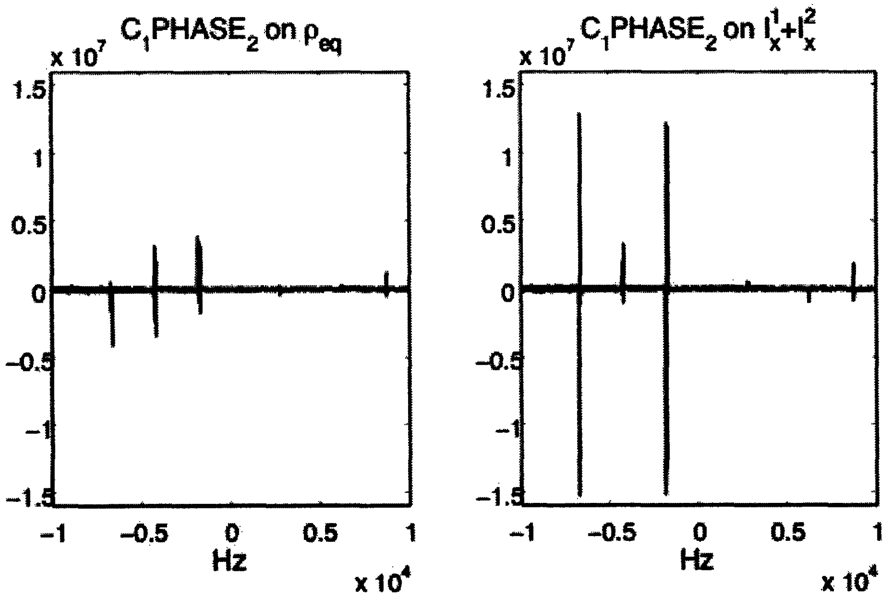

Figure 4-3: These two spectra compare the action of the $C_1 - PHASE_2$ gate on the equilibrium state and the state $I_z^1 + I_z^2$. The C-PHASE gate should have no effect on ρ_{eq} and transform the I_x state into $I_z^1 I_x^2 + I_x^1 I_z^2$. The resulting spectrum for the latter therefore contains two antiphase peaks on spins 1 and 2.

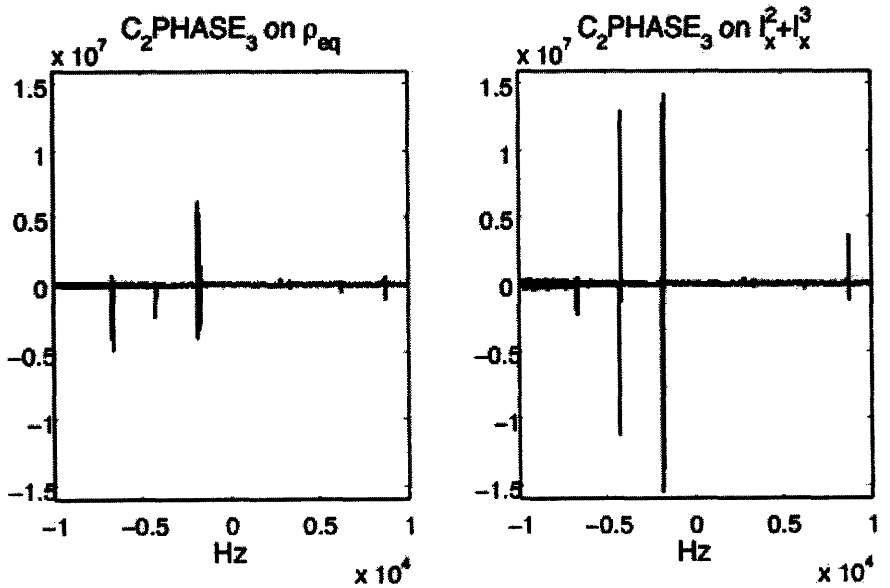

Figure 4-4: These two spectra compare the action of the $C_2 - PHASE_3$ gate on the equilibrium state and the state $I_z^2 + I_z^3$. $(C_2 - PHASE_3)\rho_{eq} = \rho_{eq}$ and $(C_2 - PHASE_3) I_z^2 + I_z^3 = I_z^2 I_x^3 + I_x^2 I_z^3$.

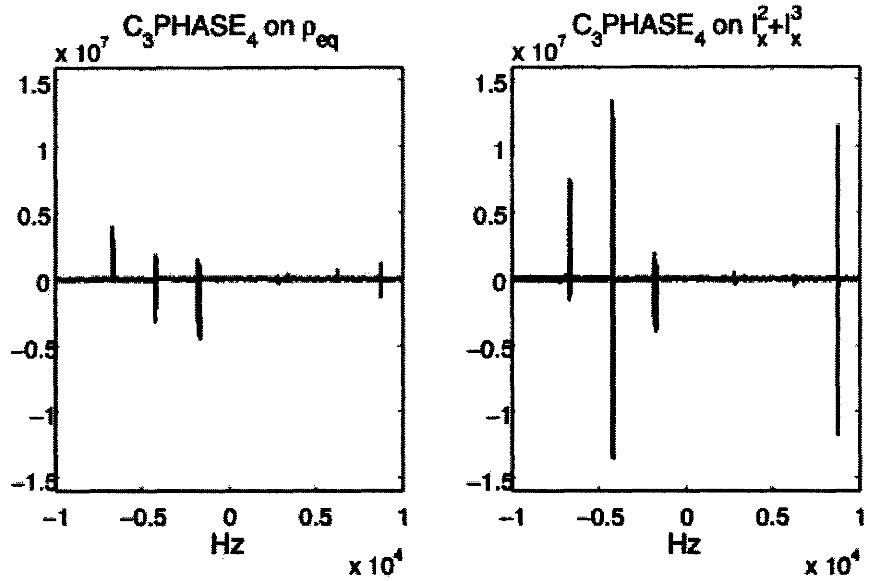

Figure 4-5: These two spectra compare the action of the $C_3 - PHASE_4$ gate on the equilibrium state and the state $I_z^3 + I_z^4$.

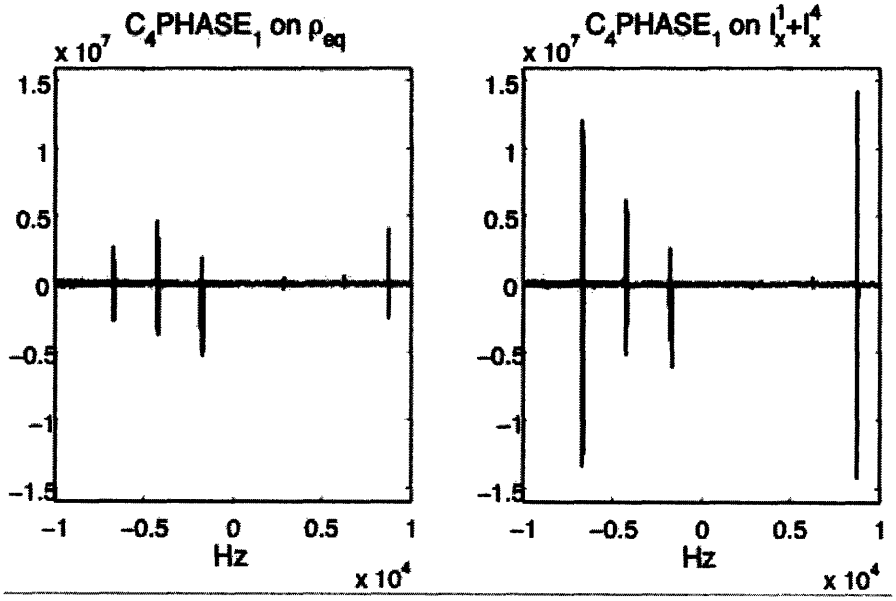

Figure 4-6: These two spectra compare the action of the $C_4 - PHASE_1$ gate on the equilibrium state and the state $I_z^1 + I_z^4$.

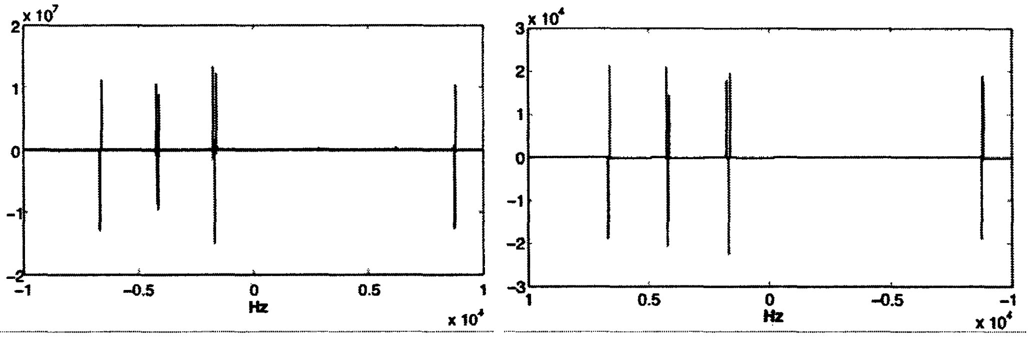

(a) Experiment

(b) Simulation

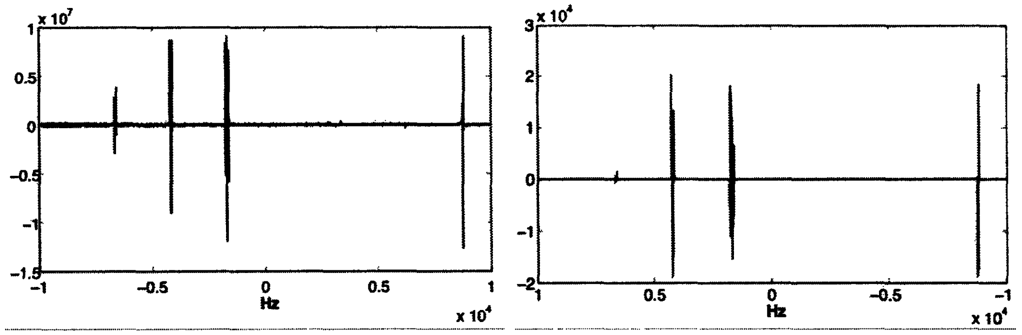

(c) Experiment

(d) Simulation

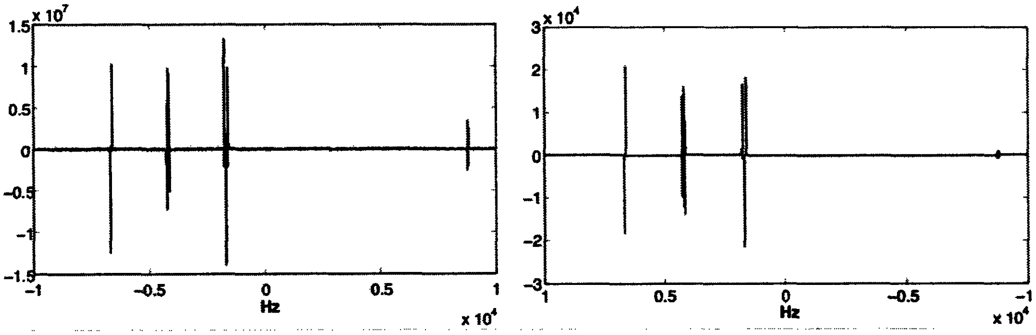

(e) Experiment

(f) Simulation

Figure 4-7: (a)-(b) show the experimental and simulated spectra of the carbon system after the linear cluster preparation has been applied to thermal equilibrium; (c)-(d) show the spectra after the linear cluster preparation was applied to the pseudo-pure state term corresponding to $I_z^1 I_z^2$, after a $\frac{\pi}{2}$ pulse along x on the first carbon. (e)-(f) show the spectra of the $I_z^3 I_z^4$ terms after the linear cluster preparation sequence and a $\frac{\pi}{2}$ pulse along x on the fourth carbon. In the next couple of figures, we provide a spin-by-spin comparison of each of the spectra with simulated results and provide the product operator expression for the states.

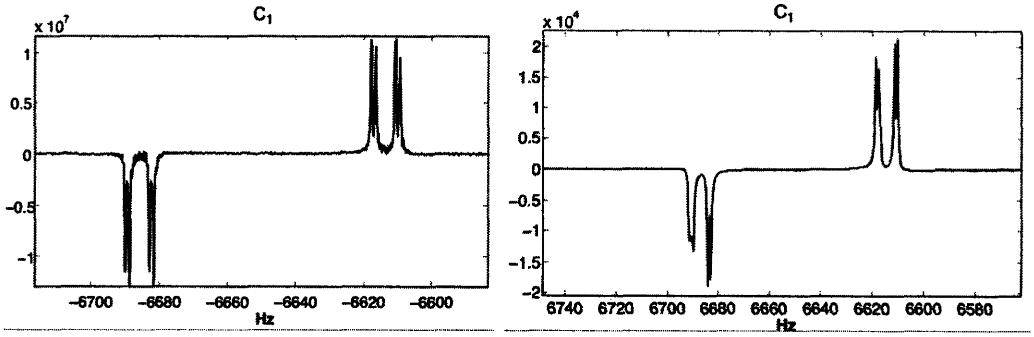

(a) Experiment (b) Simulation

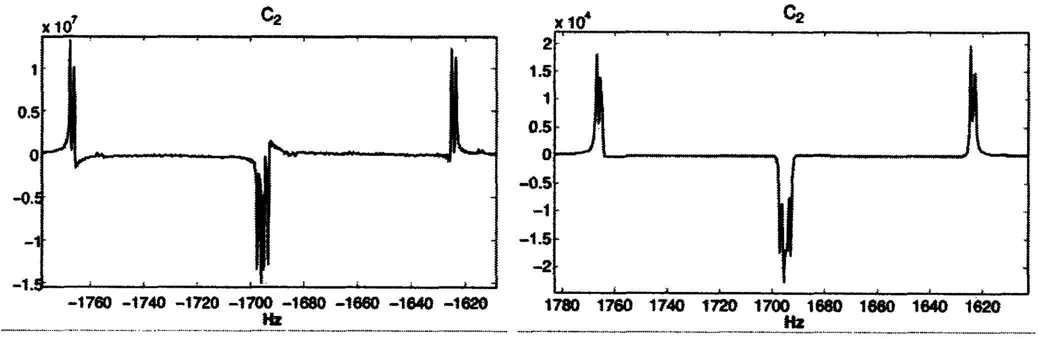

(c) Experiment (d) Simulation

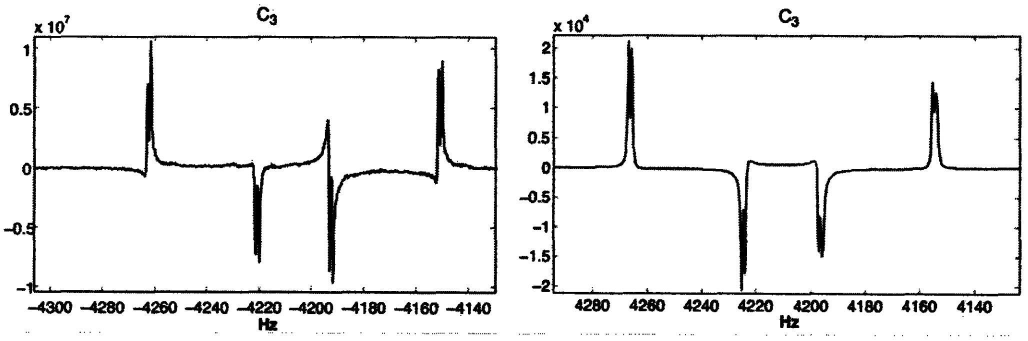

(e) Experiment (f) Simulation

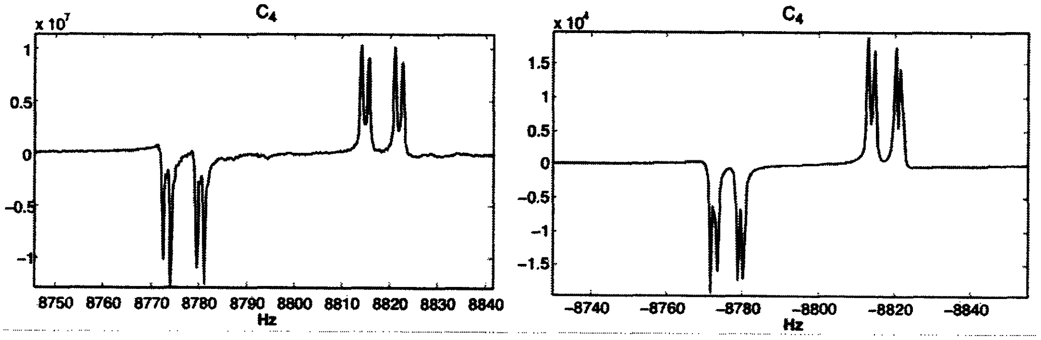

(g) Experiment (h) Simulation

Figure 4-8: Spin-by-spin comparison of the experimental detection of the state $I_x^1 I_z^2 + I_z^3 I_x^4 + I_z^1 I_x^2 I_z^3 + I_z^2 I_x^3 I_z^4$ with simulations. This state results from applying the linear cluster preparation to thermal equilibrium.

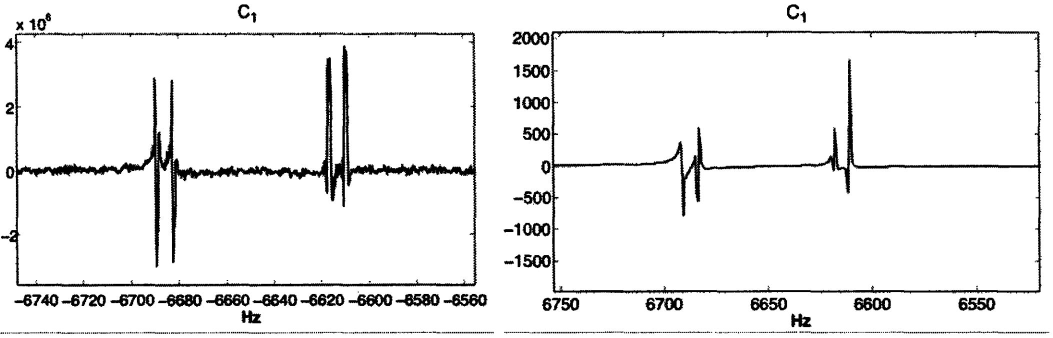

(a) Experiment (b) Simulation

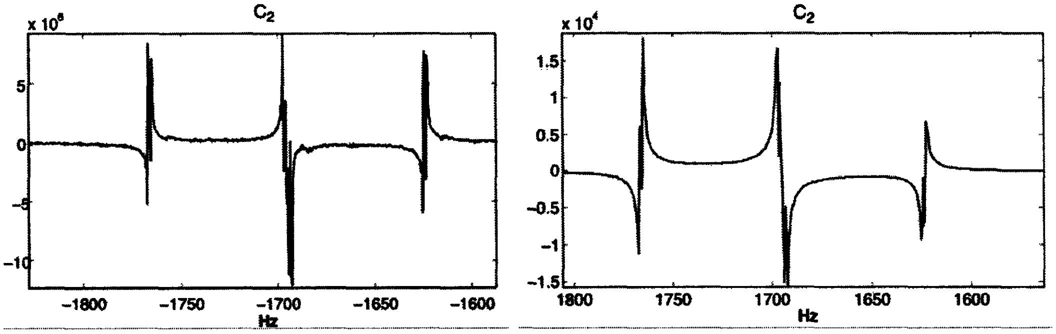

(c) Experiment (d) Simulation

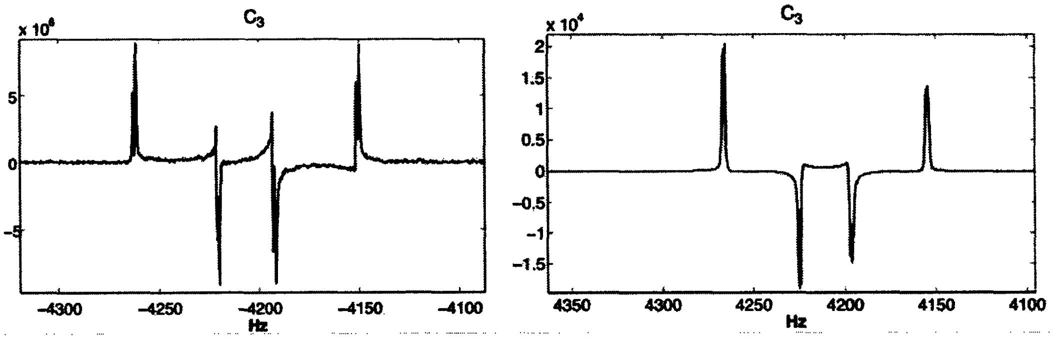

(e) Experiment (f) Simulation

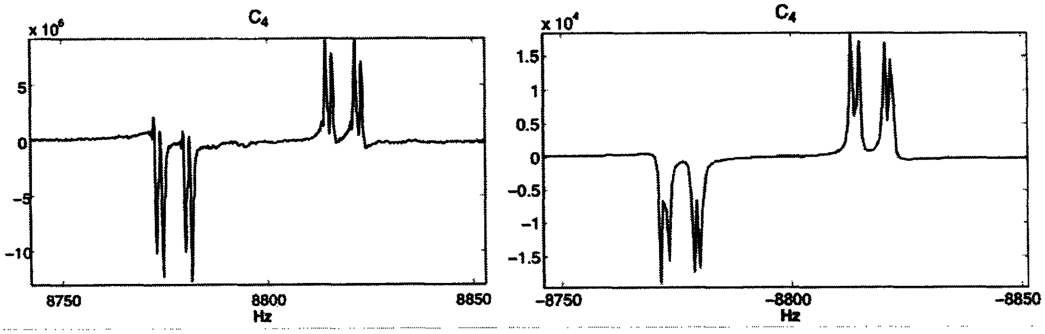

(g) Experiment (h) Simulation

Figure 4-9: Spin-by-spin comparison with simulations of the experimental measurement of the state $I_z^1 I_x^2 I_z^3 + I_z^2 I_x^3 I_z^4 + I_z^3 I_x^4 + I_y^1 I_y^2 I_z^3$, with a $\frac{\pi}{2})_x^1$ readout. The final state is $-I_y^1 I_x^2 I_z^3 + I_z^2 I_x^3 I_z^4 + I_z^3 I_x^4 + I_z^1 I_y^2 I_z^3$.

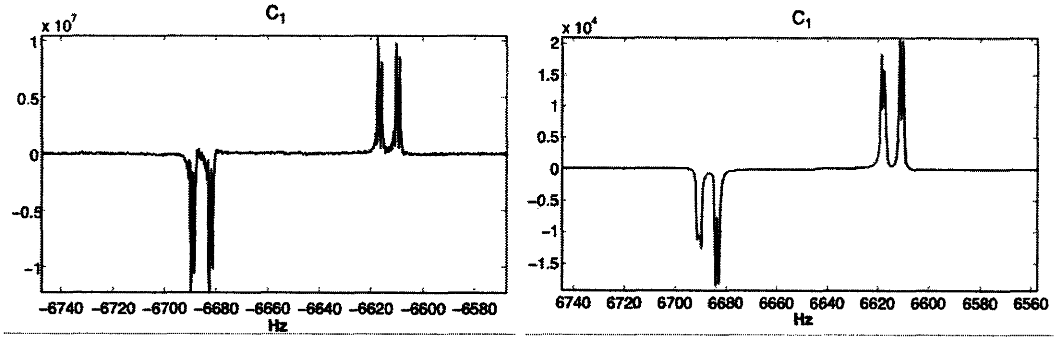

(a) Experiment

(b) Simulation

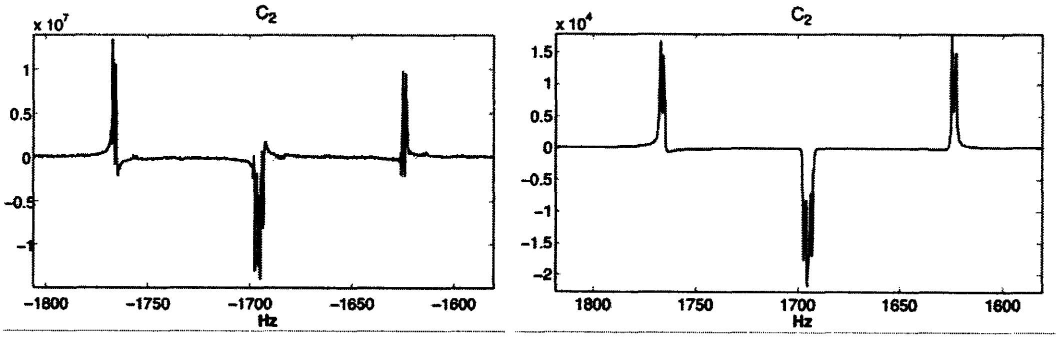

(c) Experiment

(d) Simulation

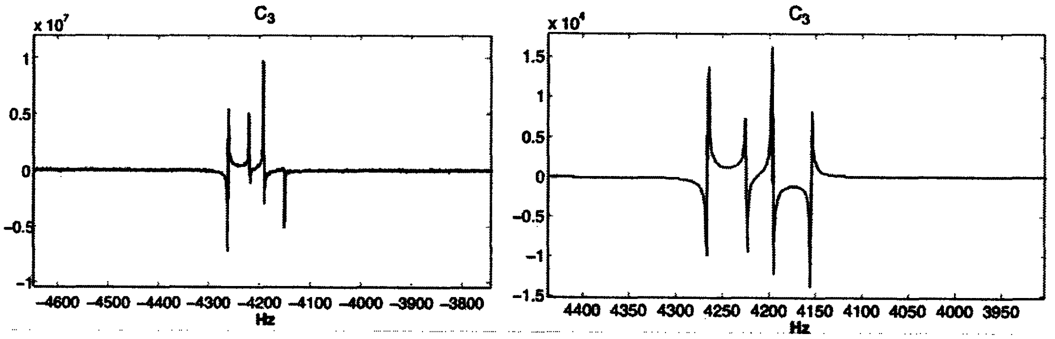

(e) Experiment

(f) Simulation

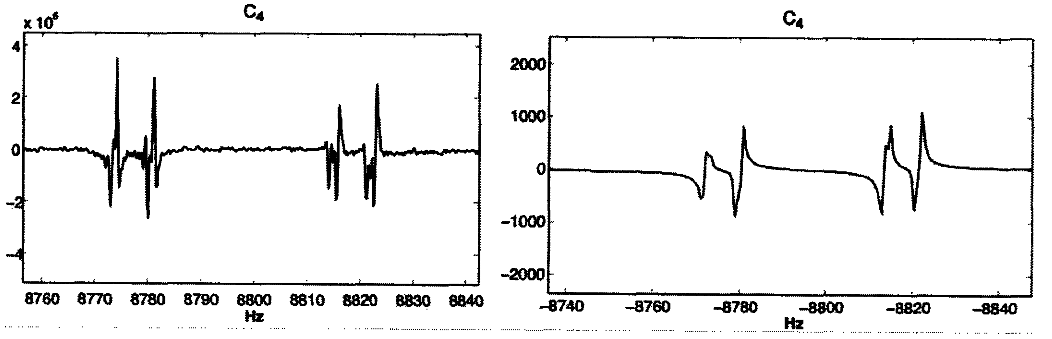

(g) Experiment

(h) Simulation

Figure 4-10: Spin-by-spin comparison with simulations of the experimental measurement of the state $I_x^1 I_z^2 + I_z^1 I_x^2 I_z^3 + I_z^2 I_x^3 I_z^4 + I_z^2 I_y^3 I_y^4$, with a $\frac{\pi}{2})_x^4$ readout. The final state is $I_x^1 I_z^2 + I_z^1 I_x^2 I_z^3 - I_z^2 I_x^3 I_y^4 + I_z^2 I_y^3 I_z^4$.

Chapter 5

Discussion

In this thesis, we first studied the entanglement properties of a four-qubit cluster-state by using a nine-parameter measure that takes into account both the global and piecewise entanglement properties of the state. The measures we used also allowed us to reveal the entanglement structure of the cluster-state under qubit losses. We found that the four-qubit cluser-state retains some true tripartite entanglement under one qubit loss, but loses all bipartite entanglement upon disposal of any two qubits. This reinforces the notion of shared or distributed entanglement in a multipartite system, since local entanglement must be nonmaximal if a state exhibits maximal global entanglement. Our results are consistent with published observations on multipartite entanglement [31].

We subsequently attempted to realize the cluster-state in a liquid NMR sample of Crotonic acid, via the use of pulses generated by the GRAPE algorithm. The GRAPE method of finding pulses presents an alternative approach to strongly modulated pulses (SMP) [34] for coherently controlling a system of qubits and implementing precise unitary transformations in NMR. There are challenges in using the GRAPE code to generate pulses, mainly because protocols for its implementation in liquid-state NMR have not yet been well-established. One difficulty we encountered is related to the finding the optimal duration of a given GRAPE pulse. We found, as in the case for the C-PHASE gates, that longer pulses are more likely to introduce errors into the operation and that varying the pulse discretization time step slightly can greatly affect the behavior of the pulse.

Another important aspect to the experiment is the preparation of a temporally averaged pseudo-pure state. The approach of creating terms in the pseudo pure state separately and computationally adding them post-experiment to yield a full state avoids the problem of observing low signals due to distributed magnetization in the spatially averaged pseudo-pure state, whose creation involves the application of RF pulses and field gradients on a single state.

For the cluster-state experiment, we created a set of pulses corresponding to both one qubit and two qubit operations and tested them on a couple of input states. We were, however, unable to detect most of the three-body terms in the pseudo-pure state, possibly due to the fact that the antiphase peaks introduced during the tomography sequence between weekly coupled carbons cannot be resolved from the finite linewidth of the spectrum. This problem must be overcome before one can calculate the appropriate weighting for each step of the pseudo-pure state preparation.

We experienced a similar problem in our attempt to measure the experimentally prepared linear cluster-state; almost every term created after applying the sequence contains three-body coherences that are difficult to detect, leading to the low correlation results. State detection was therefore inferred from spectral results, rather than constructing an experimental density matrix.

While there remain significant problems that would need to be resolved before we can fully utilize the GRAPE pulse-generated pseudo-pure state as a reliable substrate for preparing special states with high fidelities and executing quantum computational tasks, this study has presented some preliminary results that might lend insight into what some of the issues are and how one might attack them in future experiments.

Appendix A

Pseudo-Pure State Preparation via Temporal Averaging

We prepared each term in Eqn. 4.8 separately and added the results post-experiment to give a full pseudo-pure state. Additional terms that were created during preparation were eliminated from the final state by weighing the contribution from the result of each sequence with an appropriate coefficient.

State preparation was performed using GRAPE pulses, gradients, and delays. The pulse sequences and the necessary GRAPE pulses were designed and provided by Troy Borneman. Here we list the method for creating each of the pseudo pure state term as well as the expected output states (the desired terms are in bold print). All terms were prepared from thermal equilibrium.

The pulses are represented by $\theta)^i_\phi$, where θ describes the rotation angle; ϕ is the rotation axis on the x-y plane; and i denotes the carbon spin. The gradient $[grad]$ is set to 1% along the $\hat{z}$ axis.

1. $-I^1_z$:

$$\frac{\pi}{2})^{2,3,4}_x - \pi)^1_x - [grad] \tag{A.1}$$

2. $-I_z^2$:

$$\frac{\pi}{2})_x^{1,3,4} - \pi)_x^2 - [grad] \tag{A.2}$$

3. $-I_z^3$:

$$\frac{\pi}{2})_x^{1,2,4} - \pi)_x^3 - [grad] \tag{A.3}$$

4. $-I_z^4$:

$$\frac{\pi}{2})_x^{1,2,4} - \pi)_x^4 - [grad] \tag{A.4}$$

5. $I_z^2 + I_z^3 + I_z^4 + \mathbf{I_z^1 I_z^2}$:

$$\frac{\pi}{2})_y^1 - \frac{1}{2J_{12}} - \frac{\pi}{2})_{58.83^\circ}^1 - [grad] \tag{A.5}$$

6. $-I_z^1 + I_z^3 + I_z^4 + \mathbf{I_z^2 I_z^3}$:

$$\frac{\pi}{2})_y^2 - \frac{1}{4J_{23}} - \pi)_x^1 - \frac{1}{4J_{23}} - \frac{\pi}{2})_{305.569^\circ}^2 - [grad] \tag{A.6}$$

7. $I_z^1 + I_z^2 + I_z^3 + \mathbf{I_z^3 I_z^4}$:

$$\frac{\pi}{2})_y^4 - \frac{1}{2J_{34}} - \frac{\pi}{2})_{294.577^\circ}^4 - [grad] \tag{A.7}$$

8. $I_z^3 + I_z^4 - I_z^2 + \mathbf{I_z^1 I_z^3}$:[1]

$$\frac{\pi}{2})^2_y - \frac{1}{2J_2^{avg}} - \frac{\pi}{2})^2_{114.050^\circ} - \frac{\pi}{2})^1_y - \frac{1}{2J_{12}} - \frac{\pi}{2})^1_{240.788^\circ} - \pi)^2_x - [grad] \tag{A.8}$$

9. $-I_z^1 - I_z^2 - I_z^2 I_z^3 + \mathbf{I_z^2 I_z^4}$:

$$\begin{aligned}&\frac{\pi}{2})^4_y - \frac{1}{2J_{34}} - \frac{\pi}{2})^4_{294.577^\circ} - \frac{\pi}{2})^3_y - \frac{1}{4J_{23}} - \pi)^4_x - \frac{1}{4J_{23}} - \frac{\pi}{2})^3_{295.780^\circ} \\ &- \frac{\pi}{2})^2_y - \frac{1}{4J_{23}} - \pi)^1_x - \frac{1}{4J_{23}} - \frac{\pi}{2})^2_{309.574^\circ} - \pi)^3_x - [grad]\end{aligned} \tag{A.9}$$

10. $I_z^4 - I_z^1 I_z^2 - I_z^3 I_z^4 + \mathbf{I_z^1 I_z^4}$:

$$\begin{aligned}&\frac{\pi}{2})^2_y - \frac{1}{2J_2^{avg}} - \frac{\pi}{2})^2_{114.050^\circ} - \frac{\pi}{2})^1_y - \frac{1}{2J_{12}} - \frac{\pi}{2})^1_{60.788^\circ} - \frac{\pi}{2}{}^3_y - \frac{1}{4J_{34}} - \pi)^2_x \\ &- \frac{1}{4J_{34}} - \frac{\pi}{2})^3_{139.041^\circ} - \frac{\pi}{2})^4_y - \frac{1}{2J_{34}} - \frac{\pi}{2})^3_{309.763^\circ} - \pi)^3_x - [grad]\end{aligned} \tag{A.10}$$

11. $I_z^1 + I_z^3 + I_z^4 + \mathbf{I_z^1 I_z^2 I_z^3}$:

$$\frac{\pi}{2})^2_y - \frac{1}{2J_2^{avg}} - \frac{\pi}{2})^2_{114.050^\circ} - [grad] \tag{A.11}$$

12. $I_z^1 + I_z^2 - I_z^2 I_z^3 + \mathbf{I_z^2 I_z^3 I_z^4}$:

$$\frac{\pi}{2})^4_y - \frac{1}{2J_{34}} - \frac{\pi}{2})^4_{294.577^\circ} - \frac{\pi}{2})^3_y - \frac{1}{4J_{23}} - \pi)^4_x - \frac{1}{4J_{23}} - \frac{\pi}{2})^3_{294.780^\circ} - [grad] \tag{A.12}$$

---

[1] J_2^{avg} is the average J-coupling experienced by spin 2 and can be computed by taking the average between J_{12} and J_{23}

13. $I_z^1 - I_z^1 I_z^2 - I_z^1 I_z^2 I_z^3 + \mathbf{I_z^1 I_z^2 I_z^4}$:

$$\begin{aligned}&\frac{\pi}{2})_y^4 - \frac{1}{2J_{34}} - \frac{\pi}{2})_{294.577^\circ}^4 - \frac{\pi}{2})_y^3 - \frac{1}{4J_{23}}\\&- \pi)_x^4 - \frac{1}{4J_{23}} - \frac{\pi}{2})_{295.780^\circ}^3 - \frac{\pi}{2})_y^2 - \frac{1}{2J_2^{avg}} - \frac{\pi}{2})_{297.910^\circ}^2 - \pi)_x^{3,4} - [grad]\end{aligned} \quad \text{(A.13)}$$

14. $I_z^4 - I_z^1 I_z^2 + I_z^3 I_z^4 + \mathbf{I_z^1 I_z^3 I_z^4}$:

$$\frac{\pi}{2})_y^2 - \frac{1}{2J_2^{avg}} - \frac{\pi}{2})_{114.050^\circ}^2 - \frac{\pi}{2})_y^1 - \frac{1}{2J_{12}} - \frac{\pi}{2})_{240.788^\circ}^1 - \frac{\pi}{2})_y^3 - \frac{1}{4J_{34}} - \pi)_x^2 - \frac{1}{4J_{34}} - \frac{\pi}{2})_{139.041^\circ}^3 - [grad] \quad \text{(A.14)}$$

15. $I_z^1 + I_z^4 - I_z^3 I_z^4 + \mathbf{I_z^1 I_z^2 I_z^3 I_z^4}$:

$$\frac{\pi}{2})_y^2 - \frac{1}{2J_2^{avg}} - \frac{\pi}{2})_{114.050^\circ}^2 - \frac{\pi}{2})_y^3 - \frac{1}{4J_{34}} - \pi)_x^2 - \frac{1}{4J_{34}} - \frac{\pi}{2})_{323.071^\circ}^3 - \pi)_x^2 - [grad] \quad \text{(A.15)}$$

Appendix B

GRAPE Algorithm for Pulse Making

All pulses used for the preparation of the pseudo-pure and cluster states were generated using the Gradient Ascent Pulse Engineering (GRAPE) algorithm introduced by Khaneja et al. [33]. The algorithm utilizes optimal control theory to search for pulses that can maximize the coherence transfer between coupled spins as well as minimize relaxation effects during a given time step.

For the purpose of our experiment, the GRAPE code was used to find an optimal pulse for a given unitary operation (the controlled-PHASE gate, for example). A key parameter in the use of the GRAPE algorithm is the number of time steps chosen for the discretization of pulse shapes. We used a time step of either 10 μs or 25 μs for generating all pulses used in our experiment. The total duration of the pulse was set to 1 ms for single qubit unitaries and a pulse time comparable to the scalar coupling constant $(\frac{1}{2J_{ij}})$ for two-qubit operations between spins i and j. Table B.1 shows the control parameters for each GRAPE pulse used in the cluster-state creation sequence from the pseudo-pure state.

Table B.1: Control parameters input into the GRAPE algorithm.

Pulse	Time step	Total time	$\frac{1}{2J}$
Hadamard Transform	10 μs	1000 μs	-
C_1-PHASE$_2$	25 μs	7500 μs	6.89 ms
C_2-PHASE$_3$	10 μs	7500 μs	7.17 ms
C_3-PHASE$_4$	25 μs	12500 μs	12.0 ms
C_4-PHASE$_1$	25 μs	72000 μs	70.4 ms

Bibliography

[1] E. Knill, R. Laflamme, and G.J. Milburn. A scheme for efficient quantum computation with linear optics. *Nature*, pages 36–52, 2001.

[2] J-L. Brylinski and R. Brylinski. Universal quantum gates. *arXiv:quant-ph/0108062v1*, 2001.

[3] M.A. Nielsen. Cluster-state quantum computation. *arXiv:quant-ph/0504097*, 2005.

[4] D. Deutsch. Quantum computational networks. *Proc. R. Soc. London*, pages 73–90, 1989.

[5] A. Barenco, C.H. Bennett, R. Cleve, D.P. DiVincenzo, N. Margolus, P. Shor, T. Sleator, J.A. Smolin, and H. Weinfurter. Elementary gates for quantum computation. *Physical Review A*, pages 3457–3467, 1995.

[6] A. Calderbank and P.W. Shor. Good quantum error correcting codes exist. *Physical Review A*, page 1098, 1996.

[7] A. Steane. Error correcting codes in quantum theory. *Physical Review Letters*, page 793, 1996.

[8] G. Brassard, S.L. Braunstein, and R. Cleve. Teleportation as a quantum computation. *Physica D*, pages 43–47, 1998.

[9] D. Gottesman and I.L. Chuang. Demonstrating the viability of universal quantum computation using teleportation and single-qubit operations. *Nature*, pages 390–393, 1999.

[10] H.J. Briegel and R. Raussendorf. Persistent entanglement in arrays of interacting particles. *Physical Review Letters*, pages 910–913, 2001.

[11] R. Raussendorf and H.J. Briegel. Computational model underlying the one-way quantum computer. *arXiv:quant-ph/0108067 v2*, 2006.

[12] P. Dong, Z.Y. Zue, M. Yang, and Z.L. Cao. Generation of cluster states. *Physical Review A*, page 033818, 2006.

[13] D.C. Li and Z.L. Cao. Teleportation of two-particle entangled state via cluster state. *arXiv:quant-ph/0610050*, 2006.

[14] R. Raussendorf and H.J. Briegel. A one-way quantum computer. *Physical Review Letters*, pages 5188–5191, 2001.

[15] D. Deutsch. Quantum theory, the church-turing principle and the universal quantum computer. *Proceedings of the Royal Society of London A*, pages 97–117, 1985.

[16] A. Barenco, C.H. Bennett, R. Cleve, D.P. DiVincenzo, N. Margolus, P. Shor, T. Sleator, J.A. Smolin, and H. Weinfurter. Elementary gates for quantum computation. *Physical Review A*, pages 3457–3467, 1995.

[17] M. Pravia, E. Fortunato, Y. Weinstein, M.D. Price, G. Teklemariam, R.J. Nelson, Y. Sharf, S. Somaroo, C.H. Tseng, T.F. Havel, and D.G. Cory. Observations of quantum dynamics by solution-state nmr spectroscopy. *Concepts in Magnetic Resonance*, pages 225–238, 1998.

[18] D.G. Cory, A.F. Fahmy, and T.F. Havel. Ensemble quantum computing by nmr-spectroscopy. *Proceedings of the National Academy of Science U.S.A.*, page 1634, 1997.

[19] N.A. Gershenfeld and I.L. Chuang. Bulk spin resonance quantum computation. *Science*, page 350, 1997.

[20] R. Laflamme, E. Knill, D.G. Cory, E.M. Fortunato, T.F. Havel, C. Miquel, R. Martinez amd C.J. Negrevergne, G. Ortiz, M.A. Pravia, Y. Sharf, S. Sinha, R. Somma, and L. Viola. Nmr and quantum information processing. *Los Alamos Science*, pages 227–259, 2002.

[21] C.H. Bennett, H.J. Bernstein, S. Popescu, and B. Schumacher. Concentrating partial entanglement by local operations. *Physical Review A*, pages 2046–2052, 2000.

[22] W. Dur, G. Vidal, and J.I. Cirac. Three qubits can be entangled in two inequivalent ways. *Physical Review A*, page 062314, 2000.

[23] D.A. Meyer and N.R. Wallach. Global entanglement in multiparticle systems. *Journal of Mathematical Physics*, pages 4273–4278, 2002.

[24] P. Cappellaro, J. Emerson, N. Boulant, C. Ramanathan, S. Lloyd, and D.G. Cory. Entanglement assisted metrology. *Physical Review Letters*, page 020502, 2005.

[25] W.K. Wotters. Entanglement of formation and concurrence. *Quantum Information and Computation*, pages 27–44, 2001.

[26] V. Coffman, J. Kundu, and W.K. Wotters. Distributed entanglement. *Physical Review A*, page 052306, 2000.

[27] F. Verstraete, J. Dehaene, and B. De Moor. Normal forms and entanglement measures for multiparticle quantum states. *Physical Review A*, page 012103, 2003.

[28] F. Verstraete, J. Dehaene, B. De Moor, and H. Verschelde. Four qubits can be entangled in nine different ways. *Physical Review A*, page 052112, 2002.

[29] A. Wong and N. Christensen. Potential multiparticle entanglement measure. *Physical Review A*, page 044301, 2001.

[30] M.A. Nielsen and I.L. Chuang. *Quantum Computation and Quantum Information.* Cambridge University Press, Cambridge, England, 2000.

[31] J. Eisert and H.J. Briegel. The schmidt measure as a tool for quantifying multiparticle entanglement. *Physical Review A*, page 022306, 2001.

[32] N. Boulant, E.M. Fortunato, M.A. Pravia, G. Teklemariam, D.G. Cory, and T.F. Havel. Entanglement transfer experiment in nmr quantum information processing. *Physical Review A*, page 024302, 2002.

[33] N. Khaneja, T. Reiss, C. Kehlet, T. Schulte-Herbruggen, and S.J. Glaser. Optimal control of coupled spin dynamics: design of nmr pulse sequences by gradient ascent algorithms. *Journal of Magnetic Resonance*, pages 296–305, 2005.

[34] E.M. Fortunato, M.A. Pravia, N. Boulant, G. Teklemariam, T.F. Havel, and D.G. Cory. Design of strongly modulating pulses to implement precise effective hamiltonians for quantum information processing. *Journal of Chemical Physics*, pages 7599–7606, 2002.